nature portfolio

Peer Review File

Topological valley quasi-bound states in the continuum for radiatively accessible robust transport

Corresponding Author: Professor Baile Zhang

This file contains all reviewer reports in order by version, followed by all author rebuttals in order by version.

Version 0:

Reviewer comments:

Reviewer #1

(Remarks to the Author)
The manuscript 'Radiatively accessible topological valley transport via quasi-bound states in the continuum' by M. Wei, Y. Long, et al. reports on the theoretical design and experimental demonstration of topological valley quasi-bound states in the continuum (QBICs) within compound valley photonic crystals (VPCs) at terahertz frequencies. By implementing Brillouin zone (BZ) folding in a tri-period compound VPC, the authors successfully achieve radiatively accessible topological valley transport. Utilizing a time-domain terahertz near-field scanning system, the authors provide direct visualizations of the electric-field distributions, demonstrate a tunable Q-factor through geometric tuning, and verify the robustness of these states against scattering at sharp bends.

The work addresses a timely topic in topological photonics, and the methodology is robust. The clarity of the experimental data and the overall presentation are of high quality. I believe this work will have a significant impact on the community. Therefore, I recommend the manuscript for publication in Nature Communications, provided the authors address the following technical points.

Main Points
- The excitation of quasi-bound states in the continuum (QBICs) is inherently a narrowband resonance phenomenon characterized by high quality (Q) factors. However, the authors emphasize the potential for "broadband operation" in their introduction/abstract. To support this claim, the authors should provide a quantitative analysis of the coupling efficiency across a broader frequency range. Specifically, please quantify the radiation bandwidth of the QBIC mode and discuss how the transport robustness and transmission efficiency degrade when the operating frequency deviates from the resonance center (0.5050 THz).

- The core innovation of this topological valley QBIC relies on BZ folding. However, the underlying physical mechanism of this folding is not sufficiently explained in the main text or the Supplementary Information. The authors utilize a tri-period compound VPC to fold the valley edge states into the light cone. Could the authors clarify if it is feasible to achieve similar QBIC functionality using bi-period or four-period structures? What are the specific advantages of the tri-period design? Additionally, a small bandgap appears in Figs. 2(c) and 3(d-f); I suspect this is a direct consequence of band folding when $\delta w \neq 0$. Please provide a formal clarification on this point.

- The manuscript asserts that the Q-factors of the topological valley edge states scale linearly with δw^{-2}, but this claim is presented without theoretical derivation or supporting references. To ensure physical rigor, the authors should provide the details of their Q-factor calculations and a formal proof (or citation of a closely related analytical model) that justifies this $1/\delta w^2$ relationship in their specific lattice geometry.

Minor Points and Suggestions
* Figure 1: In Fig. 1(b), the visualization is somewhat unclear—could the authors explain the significance of the extensive black regions? Furthermore, while Figs. 1(c) and 1(d) use a ball-and-stick model to illustrate BZ folding, the manuscript would benefit from the inclusion of a corresponding tight-binding model to reinforce the theoretical framework. Lastly, for the tri-period compound VPC with $w_1 \neq w_2$, the resulting gap in the valley edge states (as seen in Figs. 2 and 3) should be explicitly discussed.

* Figure 2: The upper and lower topological valley QBIC bands appear to have distinct Q-factors, and the crossing points of the dispersion curves (red and blue lines) seem shifted. Is there an underlying symmetry-breaking mechanism responsible for this? I also suggest labeling specific Q-factors for a representative δw in Fig. 2(c) and ensuring that the color scales/axes for Q-values are consistent between Figs. 2(c) and 2(d) to facilitate comparison.

* Figure 3: Since field distributions are shown for specific discrete frequencies, please mark these exact frequency points on the dispersion plots in Figs. 2(d-f) to help the reader correlate the real-space and k-space data.

* Figure 4: To provide a more direct comparison with the experimental time-domain data, the simulated electric field intensity distributions should also be displayed at the corresponding time delays.

* On page 4 (line 204) and in Figs. 4(c) and 4(i), the reciprocal lattice vectors b_1 and b_2 should be formatted with standard vector symbols (e.g., $\mathbf{b}_1$, $\mathbf{b}_2$).

* On page 10 (lines 411-412), the authors mention "compound VPCs belonging to different topological Chern numbers." Since the system preserves time-reversal symmetry, the total Chern number must be zero. The authors likely mean "Valley Chern numbers" or "Valley-polarized topological charges." Please correct this terminology throughout the manuscript to maintain topological rigor.

Reviewer #2

(Remarks to the Author)
In this manuscript, the authors propose a modified photonic crystal configuration that enables free-space excitation of topological valley edge states. To achieve this, they introduce a tri-period supercell that folds the valley photonic crystal (VPC) band structure into the light cone, thereby rendering the originally non-radiative valley edge states radiatively accessible. By tuning the geometric parameter associated with the quasi-bound state in the continuum (quasi-BIC), the authors further engineer the Q factor of the resulting mode, which in turn controls its propagation length and excitation characteristics.

The manuscript addresses an interesting topic at the intersection of topological valley photonics and quasi-BIC physics. However, under the standards of Nature Communications, I find that the present work, which primarily combines band folding, quasi-BIC engineering, and valley edge states, does not yet convincingly establish a sufficiently strong level of conceptual novelty or broad impact. While the experimental implementation is technically solid, the manuscript would benefit from a clearer articulation of what fundamentally new physics is enabled beyond the integration of these existing frameworks. I therefore recommend major revision and encourage the authors to further clarify, in a revised manuscript or detailed response, the precise conceptual advance and broader significance of their approach.
Below I outline several specific points and questions that I would appreciate the authors addressing in a revised version or detailed response.
1. The Introduction does not fully set the physical picture correctly. Compared with conventional architectures employing localized auxiliary couplers, the proposed free-space coupling mechanism forces the entire edge mode to open a radiative channel by folding it into the light cone, thereby rendering the waveguide itself radiative.
Radiative accessibility and radiative loss are intrinsically linked by reciprocity: the same channel that enables excitation necessarily introduces decay. While the present approach improves accessibility, it simultaneously makes the waveguide intrinsically radiative, which runs counter to the conventional design objective of maintaining low-loss guided transport. In its current form, the manuscript does not convincingly clarify to what extent this trade-off meaningfully advances the coupling challenge described in the Introduction.
2. Clarification regarding Fig. 1
(i) In panel (b), the black regions on both sides appear unclear. It would be helpful if the authors could clarify what these regions represent.
(ii) In panel (e), it is not clear whether the plotted data are based on numerical simulations or are purely schematic. The figure appears to convey only the qualitative trend that Q increases as δw decreases, and the claimed scaling Q∝ δw^(-2)cannot be directly inferred from the plot. The authors are encouraged either to provide more quantitative information (e.g., explicit data points and fitting) to substantiate the scaling relation, or to simplify/remove this panel if it is intended to be purely schematic, in order to maintain clarity and conciseness.
3. Clarification regarding Fig. 3(d–f)
In Fig. 3(d–f), the background data behind the overlaid dispersion curves are not immediately clear. It would be helpful if the authors could explicitly explain what these background features represent,and how they should be interpreted in relation to the highlighted edge-state dispersion. A brief clarification in the caption or main text would improve the clarity of the figure.
4. Interpretation of the field intensity distributions in Fig. 3(g–l)
In Fig. 3(g–l), the spatial intensity distributions of the propagating modes are presented for different δw and frequencies. For a lossy guided mode, one would typically expect an approximately exponential decay along the propagation direction, with a characteristic length scale that can be estimated from the Q factor and group velocity, as discussed in the manuscript. However, several of the displayed field profiles appear to exhibit a two-peak structure rather than a simple monotonic exponential decay. It would therefore be helpful if the authors could clarify the physical origin of this behavior and explicitly explain how the characteristic propagation length is defined and extracted from these spatial profiles, particularly when the envelope does not follow a simple exponential form.

Reviewer #3

(Remarks to the Author)
In this manuscript, the authors propose and experimentally demonstrate topological valley quasi-bound states in the continuum (QBICs) in compound valley photonic crystals (VPCs) at terahertz frequencies. By leveraging Brillouin zone folding via geometric modulation, the authors fold topological valley edge states into the light cone, claiming to realize radiatively accessible topological light transport with robustness against sharp bends, which is visualized via time-domain terahertz near-field imaging. My detailed comments are outlined below.

Major Comments:
1. Insufficient clarification of novelty and substantive advance over prior literature
Radiatively accessible THz valley transport has been reported in previous work (e.g., Wenhao Wang et al. On-chip topological leaky-wave antenna for full-space terahertz wireless connectivity. Nat. Photon. (2026).). The core distinction of this work, as I can identify, is that the authors achieve radiative accessibility via geometric modulation and Brillouin zone folding (in a manner analogous to conventional qBICs), rather than directly designing valley edge states above the light cone as in prior reports. However, the manuscript did not explicitly demonstrate the substantive advantages of this proposed scheme over prior approaches for THz photonic applications.

2. Lack of experimental validation for the claimed QBIC properties
The defining figure of merit for qBICs is the quality (Q) factor, yet all analysis of Q factors in this manuscript is purely based on numerical simulations, with no experimental verification (direct or indirect) provided. This is a critical gap, as the entire premise of the work relies on the realization of topological valley qBICs. To validate the QBIC characteristics experimentally, the authors should at least perform one of the following: (1) Far-field angle-resolved transmission/reflection spectroscopy, the standard and widely accepted characterization method in the qBIC field, to directly extract the experimental Q factors of the demonstrated resonances; (2) Quantitative analysis of propagation loss from the near-field measurements to back-calculate the experimental Q factors. The authors themselves provide the analytical relation between propagation length L and Q factor (L=vgQ/(2πf0)) in the manuscript, which can be directly applied to the measured data.
Notably, the electric field distributions presented in Fig. 3g-i cannot be used to quantify propagation loss, and even show an unphysical increase in electric field intensity with propagation distance, which is most likely caused by reflection from the sample end facets. The authors can use time-gating on their time-domain near-field data to eliminate spurious reflections, and then quantitatively extract the intrinsic propagation loss of the topological valley qBIC modes, and thereby derive the experimental Q factors for direct comparison with simulations.

3. Lack of quantitative experimental verification of topological protection
The geometric modulation introduced in this work breaks the translational symmetry of the original lattice, which will inevitably induce mixing between counter-propagating edge states. Specifically, at kx=0, the opening of a gap indicates that the mode comprises equal (50%) contributions from the K and K' valleys; even at non-zero kx, the mode is never 100% a single valley component. This mixing directly undermines the valley Hall topological protection that is the foundation of the claimed robust transport. However, the manuscript only provides a qualitative demonstration of backscattering-free transport along a sharp bend, with no quantitative experimental evidence to validate the retention of topological protection.
Leveraging their time-resolved near-field measurements, the authors should be able to extract the momentum-space distributions of the modes at different frequencies and propagation times, quantitatively analyze the valley composition of the demonstrated states, and rigorously verify the degree to which topological protection is preserved in this system.

Specific and Technical Comments:
1. Universality of the Brillouin zone folding mechanism for arbitrary propagation directions
As shown in Fig. 2a, the authors apply geometric modulation along the x-direction to the entire bulk region, breaking translational symmetry along x. While this scheme works for valley edge states propagating along the x-direction, it is unclear whether this x-direction modulation can fold the band structures of valley edge states propagating along other directions in the same manner—for example, the bent waveguide path along the −1/2 x+3/2 y direction shown in Fig. 4. The authors must supplement theoretical analysis and numerical simulations to clarify the physical origin and universality of the Brillouin zone folding mechanism for edge states along arbitrary propagation directions.

2. Quantitative comparison between simulated and experimental Q factors for the measured samples
The authors fabricate and measure samples with δw=0.18, which corresponds to δw^−2≈30. According to the simulated results in Fig. 2e, the Q factor at this parameter should be approximately 2×10^5. The authors must explicitly report the experimentally measured Q factor for this sample, and provide a direct comparison and discussion of any discrepancies with the simulated value.

3. Quantitative analysis of Q factors from the measured dispersion bands
The experimentally measured projected dispersions in Fig. 3d-f exhibit significant linewidth broadening, which implies markedly lower Q factors than the ultrahigh values predicted in simulations. The authors should perform quantitative fitting of the measured dispersion bands to extract the experimental Q factors at different momenta, and explain the origin of the discrepancy between experimental and simulated results.

Overall, the concept of topological valley QBICs proposed in this manuscript is of some potential interest to the photonics community. However, I feel the manuscript currently has two critical shortcomings: (1) the limited novelty of this work compared to prior literature, and (2) the absence of key experimental validation for the core claims of qBIC characteristics and topological protection. Considering the rigorous standards required for publication in Nature Communications, I suggest authors to comprehensively address these problems.

Version 1:

Reviewer comments:

Reviewer #1

(Remarks to the Author)
The authors have made commendable efforts to improve their manuscripts and to reply to the concerns raised in the first review round. The manuscript now makes a more convincing case for the radiatively accessible robust transport. Considering the revisions and improvements, I am happy to recommend publication in Nature Communications. I made note of some improvement suggestions that appeared during revisions:

1, In Lines 76-81, the Hamiltonian equations are embedded in the text. For better readability, it is recommended to set these mathematical expressions as separate, numbered equation lines. c_{i}^{\dagger }, c_{i} should be the creation/annihilation operators, pleas clarify it in the maintext.

2, While plotting Qvs \delta w^{-2} linearly is perfectly fine and shows the trend, in the BIC community, it is also common to plot Q vs δw on a log-log scale to explicitly show the slope of -2. The authors might consider if a log-log inset would visually reinforce the Q\propto \delta w^{-2}scaling law.

Reviewer #2

(Remarks to the Author)
The authors have addressed all of my previous comments satisfactorily. I appreciate their careful revisions and detailed responses. I have no further concerns and recommend this manuscript for publication in Nature Communications.

Reviewer #3

(Remarks to the Author)
I appreciate the authors revision. Thr major claim of current version seems to be well supported by experimental results and analysis. I thus recommend its publication in Nature Communications.

Response Letter to Reviewers

We are grateful for your constructive comments on this manuscript (NCOMMS-26-011646).

In the text below, your comments are quoted in *Italics* and followed by our detailed response. We have also revised the manuscript and the Supplemental Material based on your comments, and these updates are highlighted in blue in the main text. In the text below, the references to these updates are highlighted in blue and also by a vertical red line in the left margin.

Response to Reviewer 1:

Reviewer 1 – General comments:

The manuscript 'Radiatively accessible topological valley transport via quasi-bound states in the continuum' by M. Wei, Y. Long, et al. reports on the theoretical design and experimental demonstration of topological valley quasi-bound states in the continuum (QBICs) within compound valley photonic crystals (VPCs) at terahertz frequencies. By implementing Brillouin zone (BZ) folding in a tri-period compound VPC, the authors successfully achieve radiatively accessible topological valley transport. Utilizing a time-domain terahertz near-field scanning system, the authors provide direct visualizations of the electric-field distributions, demonstrate a tunable Q-factor through geometric tuning, and verify the robustness of these states against scattering at sharp bends.

The work addresses a timely topic in topological photonics, and the methodology is robust. The clarity of the experimental data and the overall presentation are of high quality. I believe this work will have a significant impact on the community. Therefore, I recommend the manuscript for publication in Nature Communications, provided the authors address the following technical points.

Response from authors:

We thank you for your careful evaluation and positive comments, including that "*The work addresses a timely topic in topological photonics, and the methodology is robust. The clarity of the experimental data and the overall presentation are of high quality. I believe this work will have a significant impact on the community.*" We also appreciate your recommendation that the manuscript is suitable for publication in *Nature Communications* after we address the technical points. In the following, we address your comments point by point.

Reviewer 1 – Comment 1:

Main Points

- The excitation of quasi-bound states in the continuum (QBICs) is inherently a narrowband resonance phenomenon characterized by high quality (Q) factors. However, the authors emphasize the potential for "broadband operation" in their introduction/abstract. To support this claim, the authors should provide a quantitative analysis of the coupling efficiency across a broader frequency range. Specifically, please quantify the radiation bandwidth of the QBIC mode and discuss how the transport robustness and transmission efficiency degrade when the operating frequency deviates from the resonance center (0.5050 THz).

Response from authors:

We thank you for the constructive comment. We apologize for the misunderstanding caused by the phrase "broadband operation". In our work, Brillouin-zone folding is utilized to fold the topological edge-state dispersion into the light cone, forming a valley QBIC band. The valley QBICs distributed along this folded band have the radiative characteristics of conventional

QBICs and can be excited through different momentum components (corresponding to different incident angles) of a focused incident beam.

Therefore, our original statement of "broadband operation" was intended to describe the **radiative accessibility** of the valley QBICs over **a broad momentum range**, rather than the conventional definition of broadband operation under a fixed incident angle. The main motivation of our work is to achieve **radiative accessibility** while maintaining **robust transport**. To clarify, we have removed the phrase "broadband operation" from the revised manuscript and clarified the corresponding description.

"*To support this claim, the authors should provide a quantitative analysis of the coupling efficiency across a broader frequency range. Specifically, please quantify the radiation bandwidth of the QBIC mode and discuss how the transport robustness and transmission efficiency degrade when the operating frequency deviates from the resonance center (0.5050 THz).*"
The absolute coupling efficiency from free-space waves to the valley QBIC modes is difficult to determine experimentally. It depends on the focused beam profile, excitation position, polarization state, and the fact that most of the mode energy is confined inside the silicon slab. The relative excitation strength of the valley QBIC can be quantified from the measured near-field data.

Specifically, we define a normalized excitation coefficient $\gamma(f) = \frac{|E_{\mathrm{QBIC}}(f)|^2}{\max(|E_{\mathrm{QBIC}}(f)|^2)}$, where $|E_{\mathrm{QBIC}}(f)|^2$ denotes the measured electric-field intensity of the valley QBIC mode at frequency (f). The coefficient γ serves as a normalized measure of the radiative accessibility of the valley QBICs. Figure R1.1 shows the measured γ over a broad frequency range for compound VPCs with δw = 0.12, 0.15, and 0.18. The largest values of γ occur for valley QBICs located near the Γ point, where the radiative coupling to free-space waves is strongest. As the valley QBICs move away from the Γ point, the radiative accessibility gradually decreases, resulting in a reduced normalized coefficient.

To quantify the radiation bandwidth, we define it as the frequency range over which the normalized excitation coefficient γ remains above 50% of its peak value. The **extracted bandwidths** are **0.004 THz**, **0.008 THz**, and **0.015 THz** for $\boldsymbol{\delta w}$ **= 0.12**, **0.15**, and **0.18**, respectively, at $k_xP = -0.11983\pi$ (Figs. R1.1d to f). These results indicate that the radiation bandwidth increases with increasing δw, consistent with the enhanced radiative coupling and reduced Q factor of the corresponding valley QBICs.

As an example, a peak in γ is observed around 0.510 THz. When the operating frequency deviates from this resonance frequency, the normalized coefficient decreases rapidly because the frequency no longer matches that of the valley QBIC. Consequently, the excitation of the valley QBIC becomes weaker, leading to reduced transmitted signal intensity along the domain wall. For a sufficiently large frequency deviation, the valley QBIC can no longer be effectively excited.

We note that no peak is observed around 0.505 THz in Fig. R1.1a. This may be due to imperfections in the Gaussian beam profile of the focused terahertz spot and the excitation position, which affect the excitation efficiency of the valley QBICs.

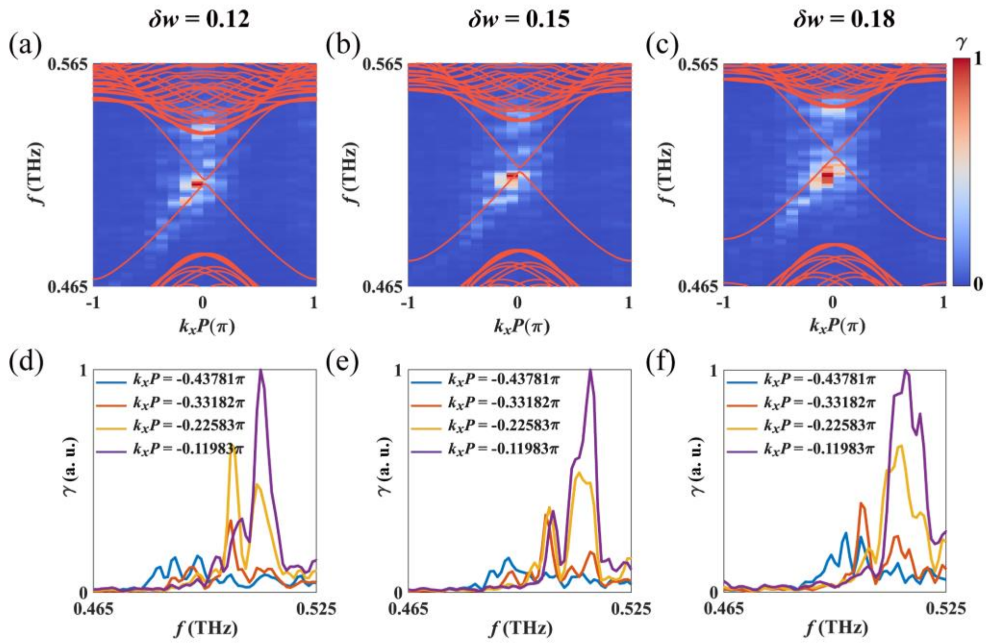

Figure R1.1 Normalized coefficient γ for the compound VPCs. (a to c) Measured normalized coefficient γ for the compound VPCs with δw = 0.12, 0.15, and 0.18, respectively. The orange lines indicate the simulated projected dispersions of the domain wall formed by corresponding compound VPCs. (d to f) Frequency-dependent normalized coefficient γ extracted at k_xP = −0.11983π, −0.22583π, −0.33182π and −0.43781π for the corresponding compound VPCs, respectively.

In summary, we have removed the phrase "broadband operation" and modified the introduction on page 2, lines 9 to 13: "Existing devices with radiative functionality have consequently exploited strongly leaky edge states for on-chip-to-free-space emission[18]. While such approaches enable efficient radiation, the associated low Q factors and short propagation lengths limit their suitability for low-loss topological transport. Achieving free-space-to-on-chip excitation while preserving robust transport therefore remains a challenge." and added the above discussion as a new Supplementary Note: "Note 5. Normalized excitation coefficient of the valley QBIC modes" in the revised Supplementary Material.

Reviewer 1 – Comment 2:

- The core innovation of this topological valley QBIC relies on BZ folding. However, the underlying physical mechanism of this folding is not sufficiently explained in the main text or the Supplementary Information. The authors utilize a tri-period compound VPC to fold the valley edge states into the light cone. Could the authors clarify if it is feasible to achieve similar QBIC functionality using bi-period or four-period structures? What are the specific advantages of the tri-period design? Additionally, a small bandgap appears in Figs. 2(c) and 3(d-f); I suspect this is a direct consequence of band folding when $\delta w \neq 0$. Please provide a formal clarification on this point.

Response from authors:

We appreciate your careful evaluation. We will address the questions point by point.

1) Feasibility of bi-period and four-period structures, and advantages of the tri-period design

Yes, similar QBIC functionality can also be achieved using bi-period and four-period structures through Brillouin-zone folding. The valley edge states of bi-period and four-period structures are also folded inside the light cone. Figure R1.2 illustrates the dispersions of the bi-period, tri-period, and four-period structures. In general, a focused incident terahertz beam contains a distribution of in-plane momentum components, k_x, with most of its energy concentrated near the Γ point, $k_x = 0$. Therefore, modes folded closer to the Γ point can be more efficiently excited by free-space illumination than modes located at larger momenta.

Compared with the bi-period structure, the tri-period structure folds a larger portion of the valley edge-state dispersion toward the Γ point, resulting in more radiatively accessible modes within the momentum range covered by the focused terahertz beam.

Compared with the four-period structure, the tri-period structure exhibits a steeper dispersion around the accessible momentum range, corresponding to a larger group velocity and more efficient on-chip propagation.

Therefore, although both bi-period and four-period structures can support valley QBICs, the tri-period structure provides a **more favorable balance** among Brillouin-zone folding, **radiative accessibility**, **momentum matching** to free-space excitation, and on-chip propagation. This balance leads to more efficient excitation and transport of the valley QBICs, which is why the tri-period compound VPC was selected in our design.

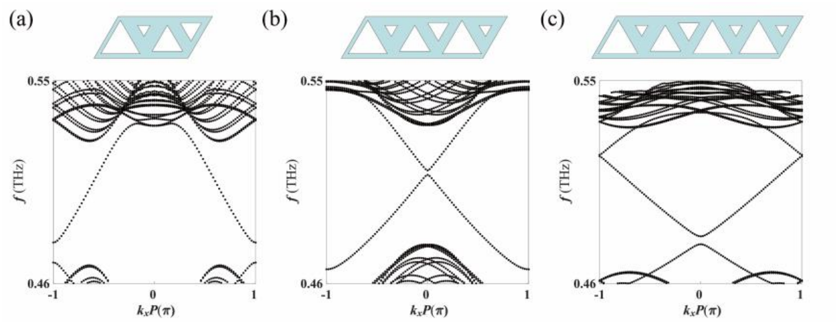

Figure R1.2 Dispersions of the bi-period, tri-period, and four-period structures, respectively.

2) Origin of the small bandgap in Figs. 2c and 3d to f
We agree that the small bandgap observed in Fig. 2c and Figs. 3d to f of the main text originates from the band-folding effect introduced when $\delta w \neq 0$. The **periodic geometric perturbation** associated with nonzero δw **breaks** the **original translational symmetry** and introduces additional **Bloch-state coupling**. As a result, states that become degenerate or nearly degenerate after Brillouin-zone folding can couple to each other, leading to an avoided crossing and the opening of a small bandgap at the folded band intersection.

This small bandgap is therefore a direct consequence of the supercell-induced Brillouin-zone folding and the finite coupling between folded Bloch states. Similar bandgap-opening phenomena induced by periodic perturbations have been reported in previous studies of folded BIC systems [S1.1].

To clarify this point, we have added the above discussion on page 3, lines 48 to 54: "The small bandgap observed in Fig. 2c and Figs. 3d to f originates from the band-folding effect introduced when $\delta w \neq 0$. The geometric perturbation associated with a nonzero δw breaks the translational symmetry of the original structure and introduces Bloch-state coupling. As a result, folded Bloch states that become degenerate or nearly degenerate can couple to each other, leading to an avoided crossing and the opening of a small bandgap. Similar bandgap-opening phenomena induced by periodic perturbations have been reported in previous studies of folded BIC systems[36]." in the revised manuscript and added a section: "Note 6. Band folding for bi-period, tri-period, and four-period" in the revised Supplementary Material.

Reviewer 1 – Comment 3:
- The manuscript asserts that the Q factors of the topological valley edge states scale linearly with δw^{-2}, but this claim is presented without theoretical derivation or supporting

references. To ensure physical rigor, the authors should provide the details of their Q-factor calculations and a formal proof (or citation of a closely related analytical model) that justifies this $1/\delta w^2$ relationship in their specific lattice geometry.

Response from authors:

We thank you for your constructive comment. We have added a supporting reference [S1.2] and demonstrated their derivation.

The coupling of guided modes to the radiative continuum is driven by the perturbation coefficient α, which controls the strength of their coupling to the radiative continuum. The quantitative relation between α and the radiative losses (i.e., radiative lifetime) can be calculated. Indeed, the coupling strength of a guided mode $\vec{E}_{\vec{k},m}(\omega,\vec{r})$ that is bound to the slab, and the external radiative continuum $\vec{E}_{ext}(\omega,\vec{r})$, is given by the overlap integral [S1.3 and S1.4]:

$$C_{\vec{k},m}(\omega) = \int \varepsilon(\vec{r})\vec{E}_{\vec{k},m}(\omega,\vec{r})\,\vec{E}^*{}_{ext}(\omega,\vec{r})d^3(\vec{r}) \tag{1}$$

where $\varepsilon(\vec{r})$ describes the permittivity of the structures. The radiative lifetime $\tau_{\vec{k},m}(\omega)$ is given by $\tau_{\vec{k},m}(\omega) \propto [C_{\vec{k},m}(\omega)]^{-2}$. The overlap integral is non-zero if there is a plane-wave component in $\vec{E}_{ext}(\omega,\vec{r})$ that is phase-matched with $\varepsilon(\vec{r})\vec{E}_{\vec{k},m}(\omega,\vec{r})$. Without the supercell-induced periodic perturbation, for a guided mode below the light cone, such a component does not exist, resulting in a dark mode $C^{dark}_{\vec{k},m}(\omega) = 0$ and $\tau^{dark}_{\vec{k},m}(\omega) = \infty$. Introducing the supercell-induced periodic perturbation causes a step change $\Delta\varepsilon$ of the permittivity over a small region of volume V, which is proportional to α. Hence the perturbed permittivity is given by:

$$\varepsilon'(\vec{r}) = \varepsilon(\vec{r}) + \delta\varepsilon(\vec{r}) \quad \text{with} \begin{cases} \delta\varepsilon = \Delta\varepsilon \;\; if \;\; \vec{r} \in \mathrm{V} \\ \delta\varepsilon = 0 \;\; if \;\; \vec{r} \notin \mathrm{V} \end{cases} \tag{2}$$

In the first-order approximation, we can assume that the perturbation does not affect the field distribution $\vec{E}_{\vec{k},m}(\omega,\vec{r})$, thus the overlap integral is given by:

$$\begin{aligned} C^{perturbed}_{\vec{k},m}(\omega) &\approx \int \varepsilon'(\vec{r})\vec{E}_{\vec{k},m}(\omega,\vec{r})\,\vec{E}^*{}_{ext}(\omega,\vec{r})d^3(\vec{r}) \\ = \int \varepsilon(\vec{r})\vec{E}_{\vec{k},m}(\omega,\vec{r})\,\vec{E}^*{}_{ext}(\omega,\vec{r})d^3(\vec{r}) &+ \Delta\varepsilon \int \vec{E}_{\vec{k},m}(\omega,\vec{r})\,\vec{E}^*{}_{ext}(\omega,\vec{r})d^3(\vec{r}) \\ &\approx \Delta\varepsilon\big[\vec{E}^*{}_{ext}(\omega,\vec{r})\vec{E}_{\vec{k},m}(\omega,\vec{r})\big] \times V \\ &\propto \alpha \end{aligned} \tag{3}$$

Consequently,

$$\tau^{perturbed}_{\vec{k},m}(\omega) \propto \alpha^{-2} \tag{4}$$

Since $Q = \omega_0\tau/2$ for a resonance at fixed frequency, the same inverse-square scaling also applies to the Q factor. This derivation explains the inverse-square dependence observed in our simulations. Physically, the geometric perturbation introduces a radiation channel with an amplitude linear in δw, while the radiative loss rate scales with the square of this coupling amplitude. Therefore, the Q factor of the valley QBIC increases as δw decreases and approaches the BIC limit as $\delta w \rightarrow 0$. Thus, the Q factors of the topological valley QBICs are proportional to δw^{-2}.

In summary, we have added the above discussion on page 4, lines 9 to 11: "The Q factor of a QBIC is known to be proportional to the inverse square of the geometric parameter δw, a relationship that is consistent across different momenta (incident angles)[22,40]." in the revised manuscript.

Reviewer 1 – Comment 4:

Minor Points and Suggestions

** Figure 1: In Fig. 1(b), the visualization is somewhat unclear—could the authors explain the* *significance of the extensive black regions? Furthermore, while Figs. 1(c) and 1(d) use a ball-and-stick model to illustrate BZ folding, the manuscript would benefit from the inclusion of a corresponding tight-binding model to reinforce the theoretical framework. Lastly, for the tri-period compound VPC with $w_1 \neq w_2$, the resulting gap in the valley edge states (as seen in Figs. 2 and 3) should be explicitly discussed.*

Response from authors:

We thank you for your constructive comment. We will address your questions point by point.

1) "*Figure 1: In Fig. 1(b), the visualization is somewhat unclear—could the authors explain the significance of the extensive black regions?*"

Figure 1b of the main text shows the experimental configuration of the sample and the terahertz near-field probe, captured by a CCD camera. As illustrated in Fig. R1.3, a circular LED array concentric with the CCD camera is used as the illumination source. The CCD records the light scattered from the sample surface and the terahertz probe, which appears as the bright regions in Fig. 1b.

The extensive black regions in Fig. 1b do not correspond to any special structural features of the sample. Instead, they arise from areas of the sample surface where the incident LED light is reflected away from the collection angle of the CCD camera. Consequently, these regions appear dark in the recorded optical image. Therefore, the contrast in Fig. 1b is mainly determined by the amount of scattered light collected by the CCD camera, rather than by the physical geometry of the sample itself.

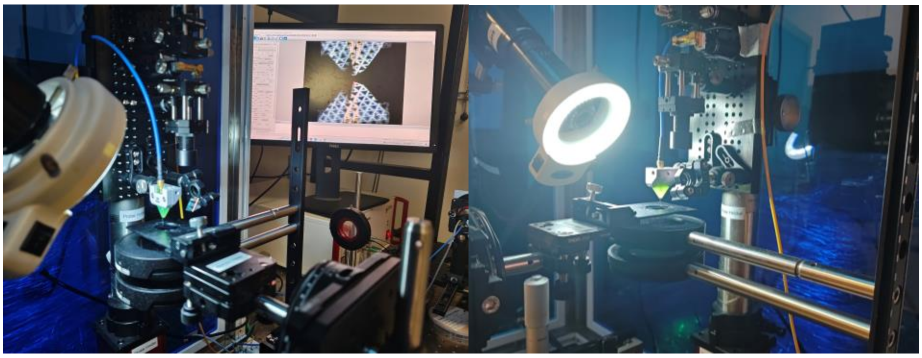

Figure R1.3 The optical images of the experimental setup. (a) The overall view of the experimental setup. (b) The side view of the circular LED array.

2) "*Furthermore, while Figs. 1(c) and 1(d) use a ball-and-stick model to illustrate BZ folding, the manuscript would benefit from the inclusion of a corresponding tight-binding model to reinforce the theoretical framework.*"

We have added the tight-binding model in the revised manuscript. A schematic configuration of a compound VPC formed by the onsite-potential modulation is illustrated in Fig. R1.4. The Hamiltonian for a VPC is $H = -t\sum_{<ij>} c_i^\dagger c_j + \sum_i U_i c_i^\dagger c_i$, where $\sum_{<ij>}$ denotes summation over nearest-neighbor pairs. The onsite potentials are defined as $U_i = \begin{cases} U_1, i = 2n \\ -U_1, \ i = 2n+1 \end{cases}$ (n represents an integer), respectively. t represents the nearest-neighbor hopping. After introducing onsite-potential modulation, the Hamiltonian for the compound VPC can be described as $H_{3P} = -t\sum_{<ij>} c_i^\dagger c_j + \sum_i U_i c_i^\dagger c_i + \sum_i \delta U_i c_i^\dagger c_i$. δU represents the strength of the onsite-potential modulation. It is defined as $\delta U_i = \begin{cases} U_1, i = 3n \\ 0, i = 3n+1 \\ -U_1, i = 3n+2 \end{cases}$. The domain wall constructed by the compound VPCs without onsite-potential modulation supports the topological valley edge states. Figure R1.4b illustrates the corresponding dispersions of the VPC and compound VPC, respectively. The onsite-potential modulation induces Brillouin-zone folding, bringing the valley edge states toward the Γ point and opening a small bandgap through Bloch-state coupling.

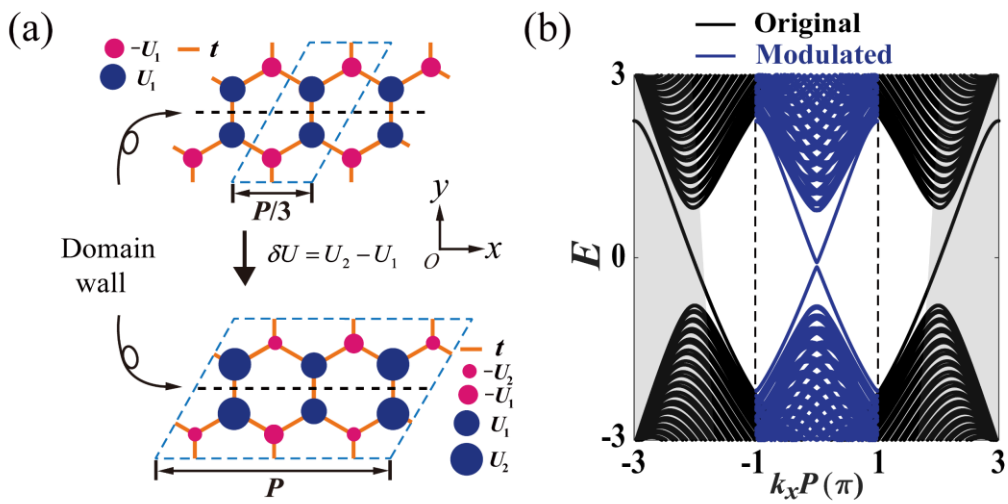

Figure R1.4 Schematic of the compound VPCs formed by onsite-potential modulation. (a) Schematic of a VPC before and after the onsite-potential modulation introduced along the domain wall. (b) The corresponding dispersions.

3) Origin of the gap in the valley edge states for the tri-period compound VPC with $w_1 \neq w_2$
This comment is related to our response to your Comment 2. The small bandgap observed in Fig. 2c and Figs. 3d to f originates from the band-folding effect introduced when $\delta w \neq 0$. The **geometric modulation** associated with a nonzero δw **breaks the translational symmetry** of the original structure and introduces additional **Bloch-state coupling**. As a result, folded Bloch states that become degenerate or nearly degenerate can couple to each other, leading to an avoided crossing and the opening of a small bandgap. Similar bandgap-opening phenomena induced by periodic perturbations have been reported in previous studies of folded BIC systems [S1.1]. This gap is therefore a direct consequence of the supercell-induced band folding and Bloch-state coupling in the compound VPC.

In summary, we have added the above discussion on page 2, lines 36 to 44: "A schematic configuration of a compound VPC formed by onsite-potential modulation is illustrated in Fig. 1c. The Hamiltonian for a VPC is $H = -t\sum_{<ij>} c_i^\dagger c_j + \sum_i U_i c_i^\dagger c_i$, where $\sum_{<ij>}$ denotes summation over nearest-neighbor pairs. The onsite potentials are defined as $U_i = \begin{cases} U_1, i = 2n \\ -U_1,\ i = 2n+1 \end{cases}$ (n represents an integer), respectively. t represents the nearest-neighbor hopping. After introducing onsite-potential modulation, the Hamiltonian for the compound VPC can be described as $H_{3P} = -t\sum_{<ij>} c_i^\dagger c_j + \sum_i U_i c_i^\dagger c_i + \sum_i \delta U_i c_i^\dagger c_i$. δU represents the strength of the onsite-potential modulation. It is defined as $\delta U_i = \begin{cases} U_1, i = 3n \\ 0, i = 3n+1 \\ -U_1, i = 3n+2 \end{cases}$. The domain wall constructed by the compound VPCs without onsite-potential modulation supports the topological valley edge states, as shown in Fig. 1d.", page 3, lines 20 to 23: "Figure 1b illustrates the experimental configuration of the sample and the terahertz near-field probe, captured by a CCD camera. The black regions correspond to areas where the incident LED light is reflected away from the CCD collection angle, making these regions appear dark in the optical image (Note 1 for details)." in the revised manuscript and added the optical image of the experimental setup to Note 1: "Note 1. The time-domain terahertz near-field scanning system" in the revised Supplementary Material.

<u>Reviewer 1 – Comment 5:</u>

** Figure 2: The upper and lower topological valley QBIC bands appear to have distinct Q factors, and the crossing points of the dispersion curves (red and blue lines) seem shifted. Is there an underlying symmetry-breaking mechanism responsible for this? I also suggest labeling specific Q factors for a representative δw in Fig. 2(c) and ensuring that the color scales/axes for Q-values are consistent between Figs. 2(c) and 2(d) to facilitate comparison.*

Response from authors:

We thank you for your constructive comment. We will address your questions point by point.

1) "*Figure 2: The upper and lower topological valley QBIC bands appear to have distinct Q factors, and the crossing points of the dispersion curves (red and blue lines) seem shifted. Is there an underlying symmetry-breaking mechanism responsible for this*"

The upper and lower topological valley QBIC bands can exhibit different Q factors because they correspond to different coupling strengths of the folded edge-state branches. After Brillouin-zone folding, the original valley edge states are brought into the reduced Brillouin zone and can couple to each other. The resulting valley QBICs have different field distributions and different overlap with the free-space radiation continuum. Therefore, their radiative coupling strengths, and hence their Q factors, can be different. This difference does not originate from an additional symmetry-breaking mechanism beyond the introduced geometric modulation. Instead, it is a natural consequence of the finite supercell perturbation and the different radiative coupling strengths of the folded valley QBICs.

Regarding the shift of the crossing points, we note that the crossing point changes only slightly, from approximately $k_xP = 0.005\pi$ to 0.015π, as δw^{-2} changes from 1 to 1000. This small shift is due to the slight variation of the effective refractive index and dispersion of the folded edge states as the geometric modulation strength changes. Consequently, it is not responsible for a symmetry-breaking mechanism. In the revision, we have refabricated the sample. The refractive index is slightly shifted from 3.22 to 3.28. The crossing points are correspondingly shifted, as illustrated in Fig. R1.5b. This shift is accounted for in the updated simulations and does not indicate an additional symmetry-breaking mechanism.

2) "*I also suggest labeling specific Q factors for a representative δw in Fig. 2(c) and ensuring that the color scales/axes for Q-values are consistent between Figs. 2(c) and 2(d) to facilitate comparison.*"

We have labeled the Q factors of the QBICs in the dispersion of a compound VPC with $\delta w = 0.12$ at $k_xP = 0.01\pi$, as illustrated in Fig. R1.5a.

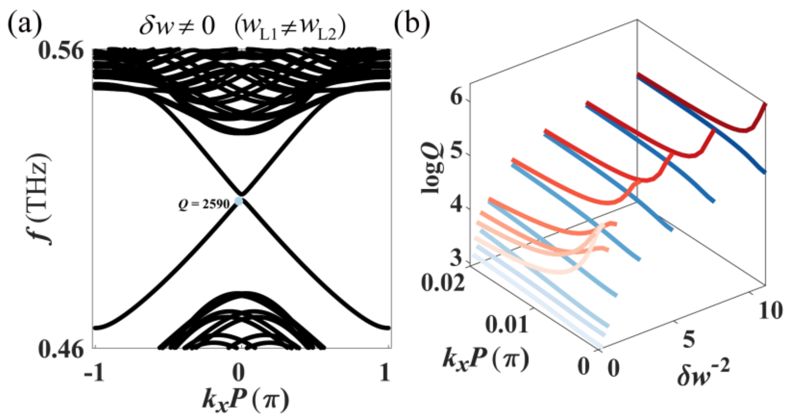

Figure R1.5 The dispersion and Q factors for the domain walls formed by compound VPCs with $\delta w = 0.12$. (a) Dispersion of the domain walls formed by the compound VPCs with $\delta w = 0.12$. (b) Dependences of the Q factors of the topological valley QBIC bands on the inverse square of the geometric parameter δw for different momenta. The blue and red lines represent the dispersion lines of the lower and upper topological valley QBIC bands, respectively.

In summary, we have updated the Figs. 2c and d in the revised manuscript.

Reviewer 1 – Comment 6:

** Figure 3: Since field distributions are shown for specific discrete frequencies, please mark these exact frequency points on the dispersion plots in Figs. 2(d-f) to help the reader correlate the real-space and k-space data.*

Response from authors:

We thank you for your constructive comment. We understand that you refer to marking the frequencies of the real-space electric-field distributions in Fig. 3 on the corresponding projected dispersion plots in Figs. 3d to f, because Figs. 2d to f show the simulated Q factors and eigenmode field distributions rather than the experimentally measured projected dispersions.

Following your suggestion, we have marked the exact frequency points corresponding to the measured real-space field distributions on the projected dispersion plots in Figs. 3d to f, as shown in Fig. R1.6. The **red**, **yellow**, **cyan**, and **blue dots** indicate **0.499 THz**, **0.503 THz**, **0.507 THz**, and **0.511** THz, respectively. These markers help directly correlate the real-space electric-field distributions with the corresponding momentum-space dispersion features.

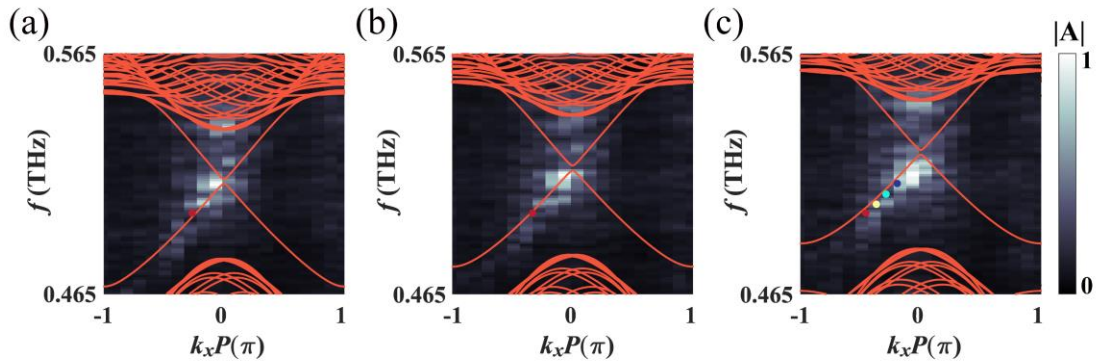

Figure R1.6 The measured projected dispersions. (a to c) The measured projected dispersions of the domain wall formed by compound VPCs with δw = 0.18 (a), 0.15 (b), and 0.12 (c), respectively. The red, yellow, cyan, and blue dots indicate 0.499 THz, 0.503 THz, 0.507 THz, and 0.511 THz, respectively.

In summary, we have updated the Figs. 3d to f in the revised manuscript.

Reviewer 1 – Comment 7:

** Figure 4: To provide a more direct comparison with the experimental time-domain data, the simulated electric-field intensity distributions should also be displayed at the corresponding time delays.*

Response from authors:

We thank you for your constructive comment. In the revision, we have fabricated and measured a Z-bend domain-wall sample to demonstrate the robust transport of the valley QBICs. Figure R1.7 illustrates the extracted simulated and experimental results at different time delays.

To provide a direct comparison with the experimental time-domain measurements, we have also extracted the simulated electric-field intensity distributions at the same time delays as those in the experiment, as illustrated in Fig. R1.7. The experiment and simulation results indicate that the valley QBIC remains well confined along the Z-bend domain wall during propagation, indicating robust transport through the sharp bends.

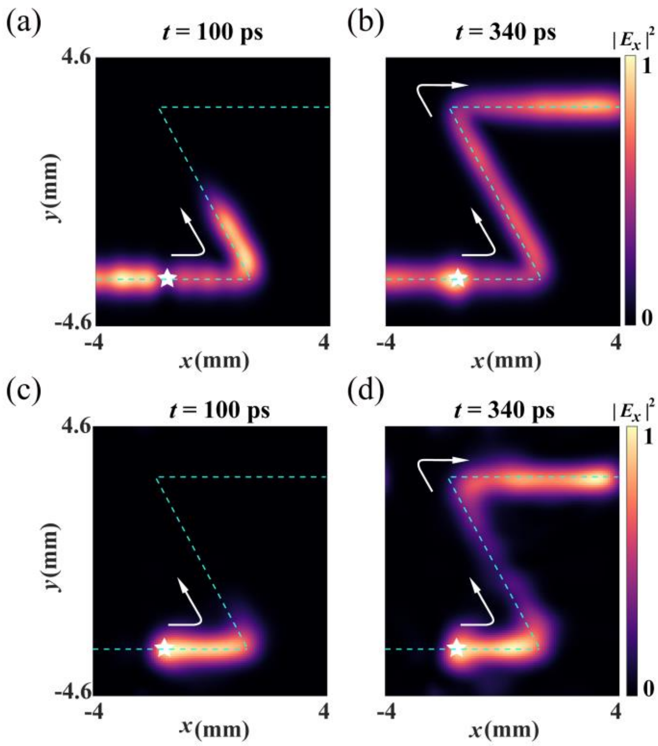

Figure R1.7 Extracted simulated and measured electric-field intensity distributions of the Z-bend domain wall in the compound VPC. (a and b) The extracted simulated electric-field intensity distributions of the topological valley QBIC mode in the Z-bend domain wall of the compound VPC with $\delta w = 0.12$ at 0.495 THz for delay times of 100 ps and 340 ps, respectively. (c and d) The extracted measured electric-field intensity distributions of the topological valley QBIC mode in the Z-bend domain wall of the compound VPC with $\delta w = 0.12$ at 0.495 THz for delay times of 100 ps and 340 ps, respectively.

In summary, we have added the simulated results and updated experimental results in the revised Fig. 4 in the revised manuscript.

Reviewer 1 – Comment 8:

** On page 4 (line 204) and in Figs. 4(c) and 4(i), the reciprocal lattice vectors b_1 and b_2 should be formatted with standard vector symbols (e.g., $\mathbf{b}_1$, $\mathbf{b}_2$).*

Response from authors:

We thank you for your constructive comment. We have changed the vector symbols.

Reviewer 1 – Comment 9:

** On page 10 (lines 411-412), the authors mention "compound VPCs belonging to different topological Chern numbers." Since the system preserves time-reversal symmetry, the total Chern number must be zero. The authors likely mean "Valley Chern numbers" or "Valley-polarized topological charges." Please correct this terminology throughout the manuscript to maintain topological rigor.*

Response from authors:

We thank you for your kind reminder. We have revised the wording in the revised manuscript on page 11, lines 19 and 20: "The red and blue regions represent compound VPCs belonging to opposite Chern numbers, respectively."

Reference

S1.1 Shi, W. *et al.* Terahertz bound states in the continuum with incident angle robustness induced by a dual period metagrating. *Photonics Res.* **10**, 810 (2022).
S1.2 Nguyen, Hai Son, *et al*. Symmetry breaking in photonic crystals: on-demand dispersion from flatband to Dirac cones. *Phys. Rev. Lett.* **120**, 066102 (2018).
S1.3 A. Yariv and P. Yeh, Photonics: Optical Electronics in Modern Communications [The Oxford Series in Electrical and Computer Engineering] Oxford University Press, Inc., 2006.
S1.4 C. Nicolaou, W. T. Lau, R. Gad, H. Akhavan, R. Schilling, and O. Levi, *Opt. Express.* **21**, 31698-31712 (2013).

Response to Reviewer 2:

<u>Reviewer 2 – General comments:</u>

In this manuscript, the authors propose a modified photonic crystal configuration that enables free-space excitation of topological valley edge states. To achieve this, they introduce a tri-period supercell that folds the valley photonic crystal (VPC) band structure into the light cone, thereby rendering the originally non-radiative valley edge states radiatively accessible. By tuning the geometric parameter associated with the quasi-bound state in the continuum (quasi-BIC), the authors further engineer the Q factor of the resulting mode, which in turn controls its propagation length and excitation characteristics.

The manuscript addresses an interesting topic at the intersection of topological valley photonics and quasi-BIC physics. However, under the standards of Nature Communications, I find that the present work, which primarily combines band folding, quasi-BIC engineering, and valley edge states, does not yet convincingly establish a sufficiently strong level of conceptual novelty or broad impact. While the experimental implementation is technically solid, the manuscript would benefit from a clearer articulation of what fundamentally new physics is enabled beyond the integration of these existing frameworks. I therefore recommend major revision and encourage the authors to further clarify, in a revised manuscript or detailed response, the precise conceptual advance and broader significance of their approach.
Below I outline several specific points and questions that I would appreciate the authors addressing in a revised version or detailed response.

<u>Response from authors:</u>

We thank you for your careful evaluation and positive comment that "*The manuscript addresses an interesting topic at the intersection of topological valley photonics and quasi-BIC physics.*" In the following, we address your comments point-by-point.

<u>Reviewer 2 – Comment 1:</u>

The Introduction does not fully set the physical picture correctly. Compared with conventional architectures employing localized auxiliary couplers, the proposed free-space coupling mechanism forces the entire edge mode to open a radiative channel by folding it into the light cone, thereby rendering the waveguide itself radiative.
Radiative accessibility and radiative loss are intrinsically linked by reciprocity: the same channel that enables excitation necessarily introduces decay. While the present approach improves accessibility, it simultaneously makes the waveguide intrinsically radiative, which runs counter to the conventional design objective of maintaining low-loss guided transport. In its current form, the manuscript does not convincingly clarify to what extent this trade-off meaningfully advances the coupling challenge described in the Introduction.

<u>Response from authors:</u>

We thank you for the comment. We agree that "*Radiative accessibility and radiative loss are intrinsically linked by reciprocity*". The purpose of our approach is not to eliminate this trade-off, but to engineer it in a controllable manner through Brillouin-zone folding.

Our approach leverages Brillouin-zone folding to bring the topological valley edge states into the light cone, thereby introducing a radiative channel for free-space excitation. However, the resulting modes are not strongly leaky modes. Instead, they are valley QBICs whose radiative coupling strength can be continuously controlled by the geometric perturbation parameter δw. As δw decreases, the radiative leakage is suppressed and the Q factor increases following the QBIC scaling, approaching the BIC limit in principle. Therefore, the **folded edge-state band** can be engineered to provide **free-space accessibility** while still maintaining sufficiently **high Q factors** for **low-loss robust on-chip transport**.

This mechanism differs from conventional localized auxiliary couplers. In those systems, free-space coupling occurs only at predefined coupling regions. In contrast, our Brillouin-zone-folding approach makes the valley QBIC band **radiatively accessible along the domain wall**, enabling more **flexible excitation positions** while retaining **controllable radiative loss**. To demonstrate this advantage, we designed and experimentally characterized a splitter architecture, showing that the free-space-excited valley QBICs can propagate and be **routed** for subsequent on-chip signal processing.

Furthermore, although the folded valley QBIC band possesses finite radiative loss in the compound VPC, the excited valley QBICs can be coupled into an adjacent unmodulated VPC region, where the edge states lie below the light cone and radiative loss is suppressed. This **radiative-to-non-radiative transition** is demonstrated in the **junction architecture**, which shows that free-space terahertz signals can be coupled into the compound VPC and subsequently transferred to a low-loss topological waveguide.

To strengthen our claim, we fabricated two additional designs to demonstrate the advantages of robust radiatively accessible transport enabled by valley QBICs.

1) On-chip beam splitter
The first design is an on-chip beam splitter, as schematically shown in Fig. R2.1a. Figures R2.1b and c show the optical image and enlarged view of the splitter sample, respectively. The measured electric-field intensity distributions split into two branches at 0.495 THz, 0.500 THz, and 0.505 THz, as shown in Figs. R2.1d to f, respectively. The split ratio is defined as $\frac{\sum |E_U^f|^2}{\sum |E_L^f|^2}$, where $|E_U^f|^2$ and $|E_L^f|^2$ represent the electric-field intensities in the upper and lower domain walls, respectively. The corresponding split ratios are 1.12, 1.18, and 1.07, respectively, indicating nearly balanced power splitting.

2) On-chip junction structure
The second design is a junction structure, in which the compound VPC with δw = 0.12 is directly connected to the unmodulated VPC with δw = 0, as schematically shown in Fig. R2.1g. This design provides a schematic demonstration of coupling a free-space terahertz signal into an on-chip VPC channel for further processing. Figures R2.1h and i show the optical image and enlarged view of the junction sample, respectively. Intensity peaks are observed around the intentionally introduced defect in the measured electric-field intensity distributions at 0.495 THz, 0.500 THz, and 0.505 THz, as shown in Figs. R2.1j to l, respectively. These peaks indicate that the free-space-excited valley QBICs are coupled from the compound VPC into the adjacent unmodulated VPC. These results indicate that free-space terahertz signals can be coupled into an on-chip VPC through our compound VPCs for subsequent signal processing.

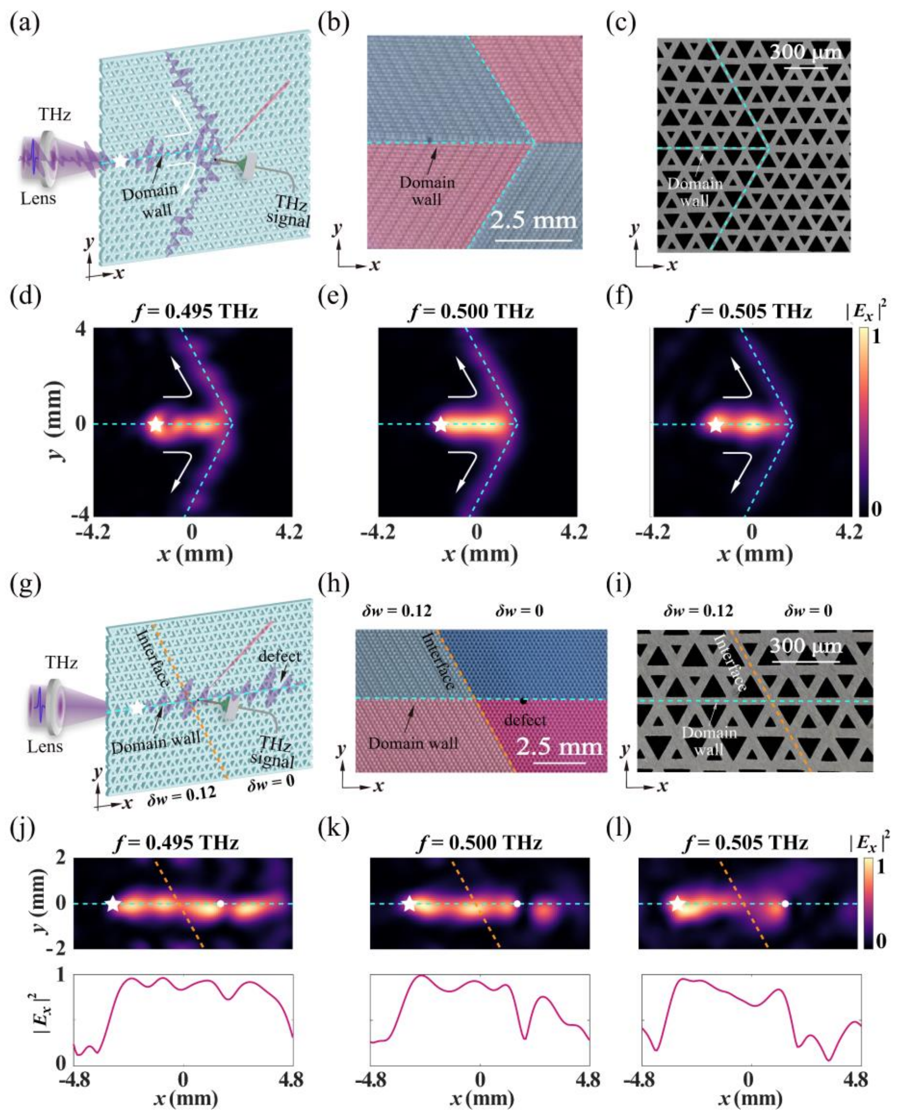

Figure R2.1 Measured electric-field intensity distributions of topological valley QBICs in the on-chip splitter and junction structures. (a) Schematic of the time-domain terahertz near-field scanning system used to record the electric-field distributions of the splitter design based on the compound VPC with δw = 0.12. (b) Optical image of the splitter sample. The red and blue regions represent compound VPCs with opposite Chern numbers. (c) Enlarged view of the splitter sample. (d to f) Measured electric-field intensity distributions of the splitter at 0.495 THz (d), 0.500 THz (e), and 0.505 THz (f). The cyan dashed lines indicate the positions of the domain walls in the compound VPCs. The white dots indicate the excitation positions. (g) Schematic of the time-domain terahertz near-field scanning system used to record the electric-field distributions of the junction between a compound VPC with δw = 0.12 and an unmodulated VPC with δw = 0. (h) Optical image of the junction sample. The red and blue regions represent VPCs with opposite Chern numbers. (i) Enlarged view of the junction sample. (j to l) Measured electric-field intensity distributions of the junction design at 0.495 THz (j), 0.500 THz (k), and 0.505 THz (l). The lower panels show the corresponding electric-field intensity profiles along the x axis at y = 0 mm.

In this sense, the proposed scheme addresses the coupling challenge not by avoiding radiation, but by controlling it, thereby enabling an integrated platform that simultaneously supports free-space routing and robust on-chip transport.

In summary, we have modified the title, abstract, and introduction to clarify our physical picture on page 1, lines 1 and 2: "Topological valley quasi-bound states in the continuum for radiatively accessible robust transport", on page 1, lines 18 to 32: "Topological valley photonics enables on-chip light transport robust against backscattering, but valley edge states typically lie outside the light cone and cannot be directly excited from free space. Existing devices with radiative functionality mainly exploit on-chip–to–free-space emission through strongly leaky modes, where enhanced radiative coupling compromises transport performance. Achieving free-space–to–on-chip excitation while preserving low-loss topological transport therefore remains a challenge. Here, we experimentally demonstrate topological valley quasi-bound states in the continuum (QBICs) in terahertz valley photonic crystals. By introducing geometric modulation and Brillouin-zone folding, valley edge states are folded into the light cone and transformed into topological valley QBICs with controllable radiative coupling while preserving robust valley transport. Using time-domain terahertz near-field imaging, we directly visualize their transport and demonstrate tunable propagation lengths together with robust transport through sharp bends. We further realize on-chip routing functionalities based on junction and splitter architectures, illustrating free-space–to–on-chip excitation and subsequent signal processing. Our work establishes topological valley QBICs as a platform for interfacing free-space radiation with low-loss topological transport, opening new opportunities for integrated terahertz devices.", page 2, lines 9 to 13: "Existing devices with radiative functionality have consequently exploited strongly leaky edge states for on-chip-to-free-space emission[18]. While such approaches enable efficient radiation, the associated low Q factors and short propagation lengths limit their suitability for low-loss topological transport. Achieving free-space-to-on-chip excitation while preserving robust transport therefore remains a challenge.", page 2, lines 20 to 23: "Integrating QBIC physics with valley topology offers a route toward modes that are simultaneously radiatively accessible and robustly guided on-chip, establishing a controllable interface between free-space radiation and topological transport.", page 2, lines 24 to 32: "Here, we experimentally demonstrate topological valley QBICs as radiative gateways for free-space-to-on-chip topological transport in terahertz compound VPCs. By introducing geometric modulation, we fold topological valley edge states into the light cone through Brillouin-zone folding and transform them into QBIC modes with controllable radiative coupling. Using time-domain terahertz near-field imaging (Figs. 1a and b), we directly visualize their real-space propagation, demonstrate geometry-tunable propagation lengths, and observe robust propagation through sharp bends. Junction and splitter architectures further show that the free-space-excited QBICs can be routed on chip for subsequent processing. Our work establishes topological valley QBICs as a platform for interfacing free-space radiation with low-loss topological transport." and added the splitter and junction design on page 5, lines 50 to 56, and page 6, lines 1 to 10: "Moreover, we fabricated two additional designs to demonstrate the advantages of robust radiatively accessible transport enabled by valley QBICs. The first design is an on-chip beam splitter, as schematically shown in Fig. 5a. Figures 5b and c show the optical image and enlarged view of the splitter sample, respectively. The measured electric-field intensity distributions split into two branches at 0.495 THz, 0.500 THz, and 0.505 THz, as shown in Figs. 5d to f, respectively. The split ratio is defined as $\frac{\sum |E_U^f|^2}{\sum |E_L^f|^2}$, where $|E_U^f|^2$ and $|E_L^f|^2$ represent the electric-field intensities in the upper and lower domain walls, respectively. The corresponding split ratios are 1.12, 1.18, and 1.07, respectively, indicating nearly balanced power splitting. The second design is a junction structure, in which the compound VPC with $\delta w = 0.12$ is directly connected to the unmodulated VPC with $\delta w = 0$, as schematically shown in Fig. 5g. This design demonstrates the process of coupling a free-space terahertz signal into an on-chip VPC channel for further signal processing. Figures 5h and i show the optical image and enlarged view of the junction sample, respectively. Intensity peaks are observed around the intentionally introduced defect in the measured electric-field intensity distributions at 0.495 THz, 0.500 THz, and 0.505 THz, as shown in Figs. 5j to l, respectively. These peaks indicate that the free-space-excited valley QBICs are coupled from the compound VPC into the adjacent unmodulated VPC. These results indicate that free-space terahertz signals can be coupled into an on-chip VPC through our compound VPCs for subsequent signal processing." and added Fig. R2.1 as Fig. 5 in the revised manuscript.

Reviewer 2 – Comment 2:
2. Clarification regarding Fig. 1
(i) In panel (b), the black regions on both sides appear unclear. It would be helpful if the authors could clarify what these regions represent.
(ii) In panel (e), it is not clear whether the plotted data are based on numerical simulations or are purely schematic. The figure appears to convey only the qualitative trend that Q increases as δw decreases, and the claimed scaling Q ∝δw^(-2)cannot be directly inferred from the plot. The authors are encouraged either to provide more quantitative information (e.g., explicit data points and fitting) to substantiate the scaling relation, or to simplify/remove this panel if it is intended to be purely schematic, in order to maintain clarity and conciseness.

Response from authors:
We thank you for your constructive comment. We will address your questions point by point.

1) "*In panel (b), the black regions on both sides appear unclear. It would be helpful if the authors could clarify what these regions represent.*"

This comment is related to our response to Reviewer 1 Comment 4. Figure 1b of the main text shows the experimental configuration of the sample and the terahertz near-field probe, captured by a CCD camera. As illustrated in Fig. R2.2 (same as Fig. R1.3), a circular LED array concentric with the CCD camera is used as an illumination source. The CCD records the light scattered from the sample surface and the terahertz probe, which appears as the bright regions in Fig. 1b.

The extensive black regions in Fig. 1b do not correspond to any special structural features of the sample. Instead, they arise from areas of the sample surface where the incident LED light is reflected away from the collection angle of the CCD camera. Consequently, these regions appear dark in the recorded optical image. Therefore, the contrast in Fig. 1b is mainly determined by the amount of scattered light collected by the CCD camera, rather than by the physical geometry of the sample itself.

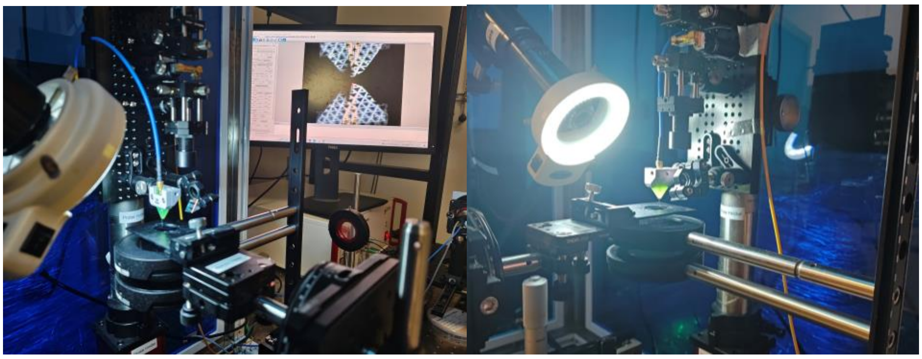

Figure R2.2 The optical images of the experimental setup. (a) The overall view of the experimental setup. (b) The side view of the circular LED array.

2) *"In panel (e), it is not clear whether the plotted data are based on numerical simulations or are purely schematic. The figure appears to convey only the qualitative trend that Q increases as δw decreases, and the claimed scaling Q ∝δw^(-2)cannot be directly inferred from the plot. The authors are encouraged either to provide more quantitative information (e.g., explicit data points and fitting) to substantiate the scaling relation, or to simplify/remove this panel if it is intended to be purely schematic, in order to maintain clarity and conciseness."*

The data presented in the original Fig. 2e were schematic. The purpose of this figure was to illustrate the trend that the Q factor increases linearly with δU^{-2}, consistent with the quasi-BIC mechanism. Following your suggestion, we have revised Fig. 2e to more clearly illustrate the qualitative trend of the Q factor as a function of δU^{-2} at different momenta, as shown in Fig. R2.3.

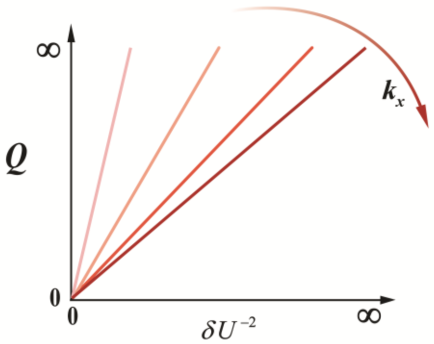

Figure R2.3 Dependences of the Q factors of the topological valley QBICs on the inverse square of the onsite-potential modulation δU at different momenta.

In summary, we have added the above discussion on page 3, lines 20 to 23: "Figure 1b illustrates the experimental configuration of the sample and the terahertz near-field probe, captured by a CCD camera. The black regions correspond to areas where the incident LED light is reflected away from the CCD collection angle, making these regions appear dark in the optical image (Note 1 for details)." and updated Fig. 2e in the revised manuscript and added the optical image of the experimental setup to Note 1: "Note 1. The time-domain terahertz near-field scanning system" in the revised Supplementary Material.

Reviewer 2 – Comment 3:

3. Clarification regarding Fig. 3(d–f)

In Fig. 3(d–f), the background data behind the overlaid dispersion curves are not immediately clear. It would be helpful if the authors could explicitly explain what these background features represent, and how they should be interpreted in relation to the highlighted edge-state dispersion. A brief clarification in the caption or main text would improve the clarity of the figure.

Response from authors:

We thank you for the constructive comment. The time-domain terahertz field-scanning imaging system records both the amplitude and phase distributions of the electric field above the sample. Based on the measured electric-field data, we perform a **two-dimensional Fourier transform** of the **spatial electric-field distributions** to obtain the experimentally measured **projected dispersions** of the domain wall formed by the compound VPCs with $\delta w = 0.18$, 0.15, and 0.12 in momentum space, as shown in Figs. R2.4a to c. In Figs. R2.4a to c, **the color maps** represent the **relative spectral intensity of the excited states** at **different frequencies and momenta**. Therefore, the background features correspond to the experimentally measured projected dispersions of the domain wall formed by the compound VPCs. The overlaid dispersion curves obtained from numerical simulations serve as a guide to identify the valley QBIC bands in the measured projected dispersions.

For example, the red dots in Figs. R2.4a to c indicate the valley QBIC at 0.499 THz for the corresponding samples. The corresponding measured electric-field distributions, shown in Figs. R2.4d to f, are localized along the domain wall, indicating that the highlighted dispersion branch originates from the valley QBICs. In contrast, other bright features outside the highlighted dispersion branch, particularly those appearing near $k_xP = 0$ at higher frequencies, are bulk modes.

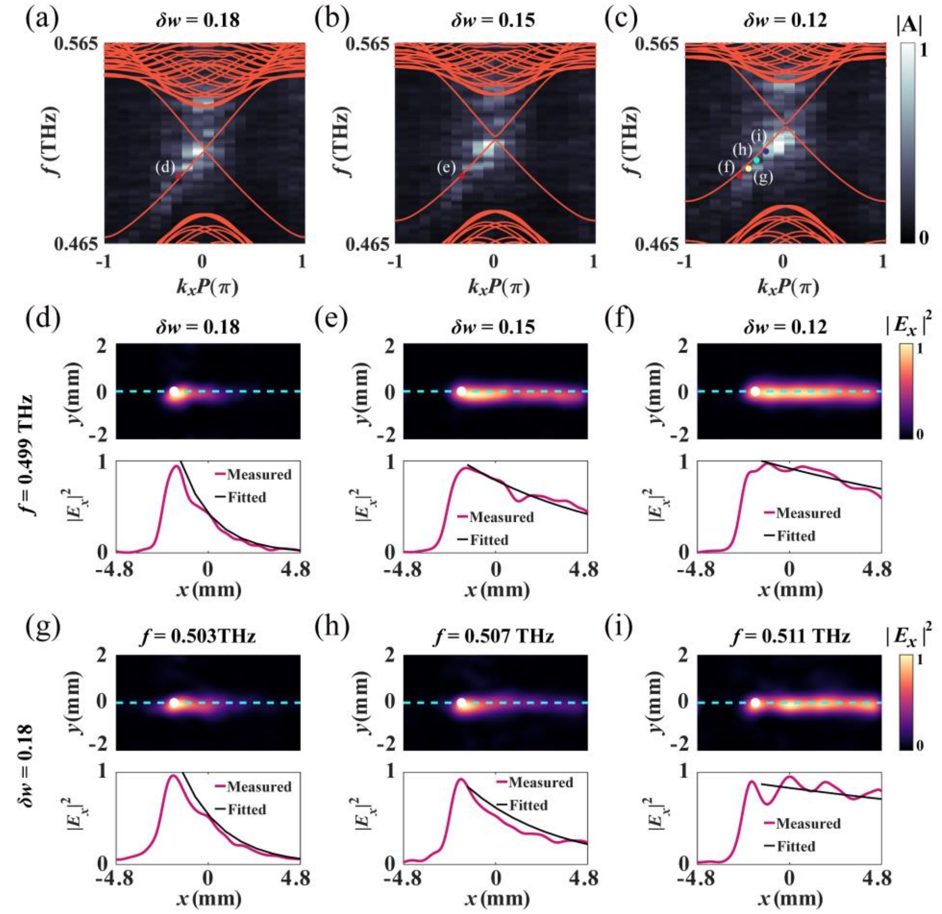

Figure R2.4 The measured projected dispersions and electric-field intensity distributions of the topological valley QBICs in the compound VPCs with different δw and corresponding fitted propagation lengths. (a to c) The measured projected dispersions of the domain wall formed by the compound VPCs with δw = 0.18 (a), 0.15 (b), and 0.12 (c), respectively. The red dots represent 0.499 THz. The yellow, cyan, and blue dots represent the 0.503 THz, 0.507 THz, and 0.511 THz, respectively. (d to f) The electric-field intensity distributions of the topological valley QBICs in our compound VPCs at 0.499 THz with δw = 0.18 (d), 0.15 (e), and 0.12 (f), respectively. The red lines in the lower panels indicate the corresponding electric-field intensity distributions of the topological valley QBICs in the corresponding compound VPCs along the x-axis at y = 0 mm, respectively. The black lines show the corresponding exponential fits used to extract the propagation lengths. (g to i) The electric-field intensity distributions of the topological valley QBICs in the compound VPC with δw = 0.18 at 0.503 THz (g), 0.507 THz (h), and 0.511 THz (i), respectively. The red lines in the lower panels indicate the corresponding electric-field intensity distributions of the topological valley QBICs in the corresponding compound VPCs along the x-axis at y = 0 mm, respectively. The black lines are the corresponding fitted results to extract the propagation length

In summary, we have added the corresponding description on page 4, lines 26 to 40: "The time-domain terahertz field-scanning imaging system records both the amplitude and phase distributions of the electric field above the sample. Based on the measured electric-field data, we perform a two-dimensional Fourier transform of the spatial electric-field distributions to obtain the experimentally measured projected dispersions of the domain walls formed by the compound VPCs with δw = 0.18, 0.15, and 0.12 in momentum space, as shown in Figs. 3d to f. In Figs. 3d to f, the color maps represent the relative spectral intensity of the excited states at different frequencies and momenta. Therefore, the background features correspond to the experimentally measured projected dispersions of the domain wall formed by the compound VPC. The overlaid dispersion curves obtained from numerical simulations serve as a guide to identify the valley QBIC bands in the measured projected dispersions. For example, the red dots in Figs. 3d to f indicate the valley QBIC at 0.499 THz for the corresponding samples. The corresponding measured electric-field distributions, shown in Figs. 3g to i, are localized along the domain wall, indicating that the highlighted dispersion branch originates from the valley QBICs. In contrast, other bright features outside the highlighted dispersion branch, particularly those appearing near $k_xP = 0$ at higher frequencies, are bulk modes." in the revised manuscript.

Reviewer 2 – Comment 4:

4. Interpretation of the field intensity distributions in Fig. 3(g–l)

In Fig. 3(g–l), the spatial intensity distributions of the propagating modes are presented for different δw and frequencies. For a lossy guided mode, one would typically expect an approximately exponential decay along the propagation direction, with a characteristic length scale that can be estimated from the Q factor and group velocity, as discussed in the manuscript. However, several of the displayed field profiles appear to exhibit a two-peak structure rather than a simple monotonic exponential decay. It would therefore be helpful if the authors could clarify the physical origin of this behavior and explicitly explain how the characteristic propagation length is defined and extracted from these spatial profiles, particularly when the envelope does not follow a simple exponential form.

Response from authors:

We thank you for your constructive comment. We will address your concerns point by point below.

1) Origin of the two-peak structures and field fluctuations

We agree that "*For a lossy guided mode, the overall field intensity is expected to exhibit an approximately exponential decay along the propagation direction*". In the measured near-field distributions, **local two-peak features** and intensity fluctuations appear due to several **experimental factors**.

First, **fabrication imperfections** may introduce local defects along the domain wall, resulting in local scattering and field enhancement. Second, the original **etching depth of 280 μm** was much larger than the designed depth of 150 μm, which can lead to nonuniform etching and position-dependent side-etching effects across the sample. These effects modify the local geometry and influence the scattering loss of the edge states. Third, since one near-field scan typically takes approximately 16 hours, **dust deposition** on the sample surface and long-term experimental fluctuations may also affect the measured field intensity.

2) Definition and extraction of the characteristic propagation length

To obtain more reliable field distributions for propagation-length extraction, we refabricated the samples by reducing the **etching depth from 280 μm to 180 μm** to suppress side-etching effects. We also optimized the near-field measurement system and performed measurements. The improved measured electric-field intensity distributions are shown in Figs. R2.4d to i. The propagation length is extracted from the measured near-field distributions by fitting the electric-field intensity profile along the propagation direction. We fit the propagation length using $|E(x)|^2 \propto \exp(-x/L)$, where x is the coordinate and L is the propagation length. The corresponding Q factor is then obtained as $Q = 2\pi f_0 L/v_g$, where f_0 is the operating frequency and v_g is the group velocity. The group velocity is extracted from the simulated dispersion because the measured projected dispersions are consistent with the simulated ones.

For the compound VPCs with $\delta w = 0.18$, 0.15, and 0.12 at 0.499 THz, the **fitted propagation lengths** are **1.73 mm**, **7.64 mm**, and **17.22 mm**, respectively, as shown in Figs. R2.4d to f. The corresponding **retrieved *Q* factors** are **119.43**, **456.86**, and **958.8**9, respectively. For the compound VPC with $\delta w = 0.18$, the fitted **propagation lengths** at 0.503 THz, 0.507 THz, and 0.511 THz are **2.20 mm**, **4.64 mm**, and **30.53 mm**, respectively, as shown in Figs. R2.4g to i. The corresponding **retrieved *Q* factors** are **143.48**, **291.45**, and **1864.30**, respectively.

These results show that the overall propagation length and retrieved Q factor increase as the perturbation strength δw decreases, consistent with the QBIC behavior.

In summary, we have added the corresponding description on page 4, lines 45 to 49: "We extract the propagation lengths from the measured near-field distributions by fitting the electric-field intensity profile along the propagation direction. We fit the propagation length using $|E(x)|^2 \propto \exp(-x/L)$, where x is the coordinate and L is the propagation length. The fitted propagation lengths are 1.73 mm, 7.64 mm, and 17.22 mm for δw = 0.18, 0.15, and 0.12 at 0.499 THz, respectively.", and page 5, lines 5 to 8: "Figures 3j to l illustrate the electric-field intensity distributions of the topological valley QBICs in the compound VPC with δw = 0.18 at 0.503 THz, 0.507 THz, and 0.511 THz, respectively. The corresponding fitted propagation lengths are 2.20 mm, 4.64 mm, and 30.53 mm, respectively." and updated Fig. 3 in the revised manuscript.

Reference

S2.1 Wei, M., Long, Y., Wu, F., Liu, G.-G. & Zhang, B. Abrupt lateral beam shifts from terahertz quasi-bound states in the continuum. *Sci. Bull.* **70**, 882–888 (2025).

Response to Reviewer 3:

Reviewer 3 – General comments:

In this manuscript, the authors propose and experimentally demonstrate topological valley quasi-bound states in the continuum (QBICs) in compound valley photonic crystals (VPCs) at terahertz frequencies. By leveraging Brillouin-zone folding via geometric modulation, the authors fold topological valley edge states into the light cone, claiming to realize radiatively accessible topological light transport with robustness against sharp bends, which is visualized via time-domain terahertz near-field imaging. My detailed comments are outlined below.

Response from authors:

We thank you for your review efforts and comments. In the following, we address your comments point-by-point.

Reviewer 3 – Comment 1:

Major Comments:

1. Insufficient clarification of novelty and substantive advance over prior literature

Radiatively accessible THz valley transport has been reported in previous work (e.g., Wenhao Wang et al. On-chip topological leaky-wave antenna for full-space terahertz wireless connectivity. Nat. Photon. (2026).). The core distinction of this work, as I can identify, is that the authors achieve radiative accessibility via geometric modulation and Brillouin-zone folding (in a manner analogous to conventional qBICs), rather than directly designing valley edge states above the light cone as in prior reports. However, the manuscript did not explicitly demonstrate the substantive advantages of this proposed scheme over prior approaches for THz photonic applications.

Response from authors:

We thank you for your review effort and comment. Our approach begins with non-radiative valley edge states below the light cone and introduces radiative accessibility through controlled Brillouin-zone folding. This mechanism is fundamentally different from the approach reported by Wang *et al.* [S3.1], where the valley edge states are directly engineered above the light cone and therefore operate as leaky modes. In contrast, our Brillouin-zone-folding scheme introduces a tunable radiative channel through a weak geometric perturbation, while retaining the low-loss transport characteristics of valley edge states. The resulting valley QBICs can exhibit high and controllable Q factors, enabling **free-space accessibility** together with **on-chip transport**. Moreover, our mechanism is based on supercell-induced symmetry engineering and band folding, rather than a specific leaky-wave dispersion design, making it applicable to a broad class of valley photonic systems.

To quantitatively demonstrate the advantages of our approach, we have performed additional simulations and experiments, including: (1) Comparison with the Type-A design reported in Ref. [S3.1], where the valley edge states are intrinsically leaky and exhibit **strong radiative loss**, resulting in a **limited propagation length** along the domain wall; (2) Junction and splitter architectures, which demonstrate **free-space-to-on-chip excitation** followed by **on-chip signal routing** and coupling to a **low-loss topological waveguide** for subsequent processing.

1) Comparison with the Type-A design reported in Ref. [S3.1]

In previous work, radiatively accessible terahertz valley states were demonstrated for on-chip-to-free-space radiation. In that design, the valley edge states were engineered to lie above the light cone, resulting in intrinsically leaky modes. Consequently, the valley edge states exhibit relatively low Q factors and short propagation lengths, which are advantageous for efficient out-coupling from the chip to free space and enable operation as a terahertz leaky-wave antenna. To quantitatively compare the radiation characteristics, we performed additional simulations and experiments based on the Type-A design reported in Ref. [S3.1]. The Type-A structure consists of a VPC with a lattice constant of a = 300 μm and two triangular air holes with side lengths of 0.88a and 0.33a, respectively. In our fabricated samples, the silicon thickness was reduced from 220 μm to 150 μm, leading to an approximately 0.021 THz shift in the valley edge-state dispersion, as shown in Figs. R3.1a and b. The simulated Q factor changes from approximately 85.94 to 70.41, indicating that the structure remains in a strongly radiative regime.

As shown in Figs. R3.1d to f, the simulated electric-field distributions at 0.33, 0.34, and 0.35 THz show rapid radiation away from the waveguide, consistent with the design principle of a leaky-wave antenna. The corresponding propagation lengths are extracted from exponential fitting of the electric-field intensity profiles using $|E(x)|^2 \propto \exp(-x/L)$, where x and L denote the coordinate and the characteristic propagation length, respectively. The extracted simulated propagation lengths are 0.61 mm, 1.94 mm, and 3.70 mm, respectively. The experimentally measured propagation lengths are 0.64 mm, 1.16 mm, and 2.82 mm, as shown in Figs. R3.1g to i, respectively. The slight discrepancies are attributed to experimental noise, finite signal-to-noise ratio, and fluctuations in the measured near-field intensity profiles.

Overall, these results confirm that the Type-A valley edge states operate in a strongly radiative leaky-wave regime with comparatively short propagation lengths, which is suitable for free-space radiation but less suitable for long-distance on-chip valley transport. In contrast, our work aims to achieve **free-space accessibility** while **preserving robust on-chip transport** through Brillouin-zone-folding-induced valley QBICs. This mechanism introduces a controllable radiative channel through a weak periodic geometric perturbation, enabling a tunable balance between free-space coupling and low-loss topological propagation.

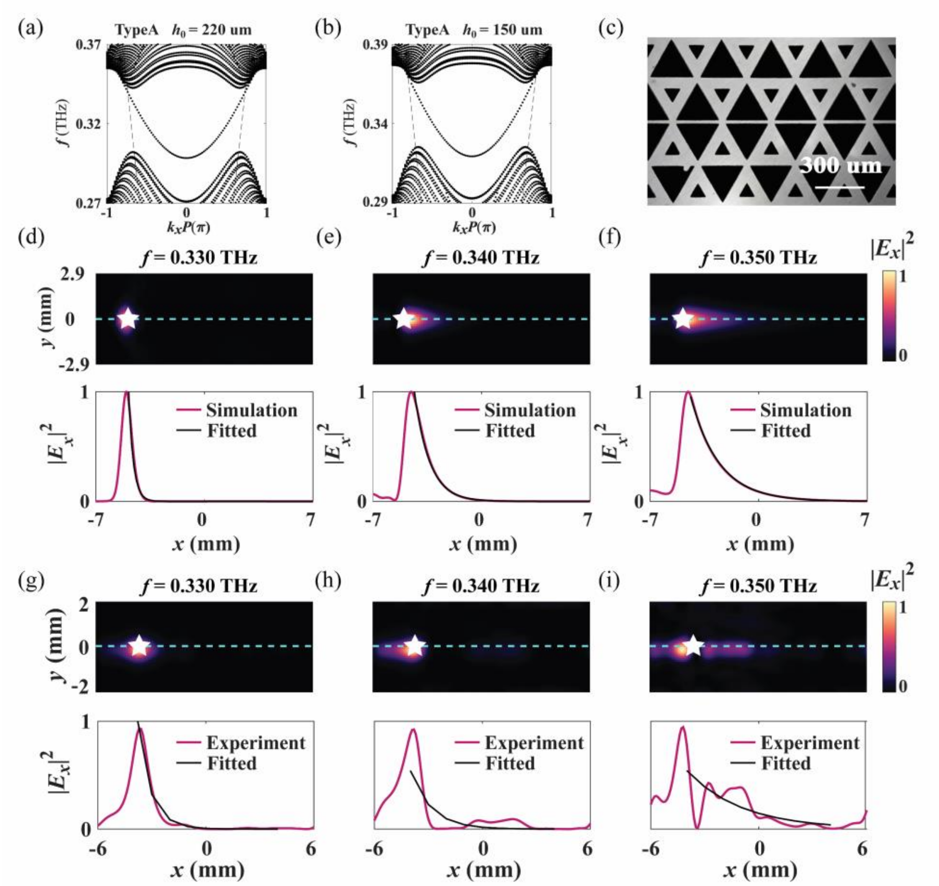

Figure R3.1 The simulated and measured results of the Type-A design. (a and b) The simulated dispersions of the Type-A design with the thicknesses of 220 μm and 150 μm, respectively. (c) The optical image of the fabricated Type-A sample with a thickness of 150 μm. (d to f) The simulated electric-field intensity distributions of the Type-A design's valley edge states at 0.33 THz, 0.34 THz, and 0.35 THz, respectively. The lower panels show the corresponding electric-field intensity distributions of the Type-A valley edge states along the x-axis at y = 0 mm, respectively. The black lines show the corresponding exponential fits used to extract the propagation lengths. (g to i) The corresponding measured electric-field intensity distributions of the Type-A design. The lower panels show the corresponding electric-field intensity distributions of the Type-A valley edge states along the x-axis at y = 0 mm, respectively. The black lines show the corresponding exponential fits used to extract the propagation lengths. The electric-field intensity distributions are normalized by the maximum absolute value of the electric-field intensities in the corresponding figures.

2) Splitter and junction architectures

In our design, by tuning δw, the Q factors of the valley QBIC modes can be sufficiently large to support long-distance propagation, thereby enabling free-space-to-on-chip coupling and subsequent terahertz signal processing. As discussed in our response to Reviewer 2 Comment 1, we further demonstrate two representative functionalities to highlight the advantages of valley QBIC transport, as shown in Fig. R3.2.

The first design is a widely used on-chip beam splitter, as schematically illustrated in Fig. R3.2a. Figures R3.2b and c show the optical image and enlarged view of the splitter sample, respectively. As shown in Figs. R3.2d to f, the measured electric-field intensity distributions at 0.495 THz, 0.500 THz, and 0.505 THz are clearly split into two branches, as expected. To quantify the splitting performance, we define the split ratio as $\frac{\sum |E_U^f|^2}{\sum |E_L^f|^2}$, where $|E_U^f|^2$ and $|E_L^f|^2$ represent the electric-field intensities in the upper and lower domain-wall branches, respectively.

The corresponding split ratios are 1.12, 1.18, and 1.07 at 0.495 THz, 0.500 THz, and 0.505 THz, respectively, demonstrating nearly balanced power splitting.

The second design is a junction architecture, in which the compound VPC with δw = 0.12 is directly connected to the unmodulated VPC with δw = 0, providing a schematic demonstration of coupling a free-space terahertz signal into an on-chip VPC for subsequent signal processing, as illustrated in Fig. R3.2g. Figures R3.2h and i show the optical image and enlarged view of the junction sample, respectively. Intensity peaks are observed around the intentionally introduced defect in the measured electric-field intensity distributions at 0.495 THz, 0.500 THz, and 0.505 THz, as shown in Figs. R3.2j to l, respectively. These peaks indicate that the free-space-excited valley QBICs are coupled from the compound VPC into the adjacent unmodulated VPC. These results indicate that free-space terahertz signals can be coupled into an on-chip VPC through our compound VPCs for subsequent signal processing.

Therefore, compared with strongly radiative leaky-wave valley states, the valley QBIC platform demonstrated here not only enables **free-space accessibility**, but also preserves sufficiently long-distance **transport** for on-chip routing and processing, which constitutes a substantive advantage for integrated terahertz photonic applications.

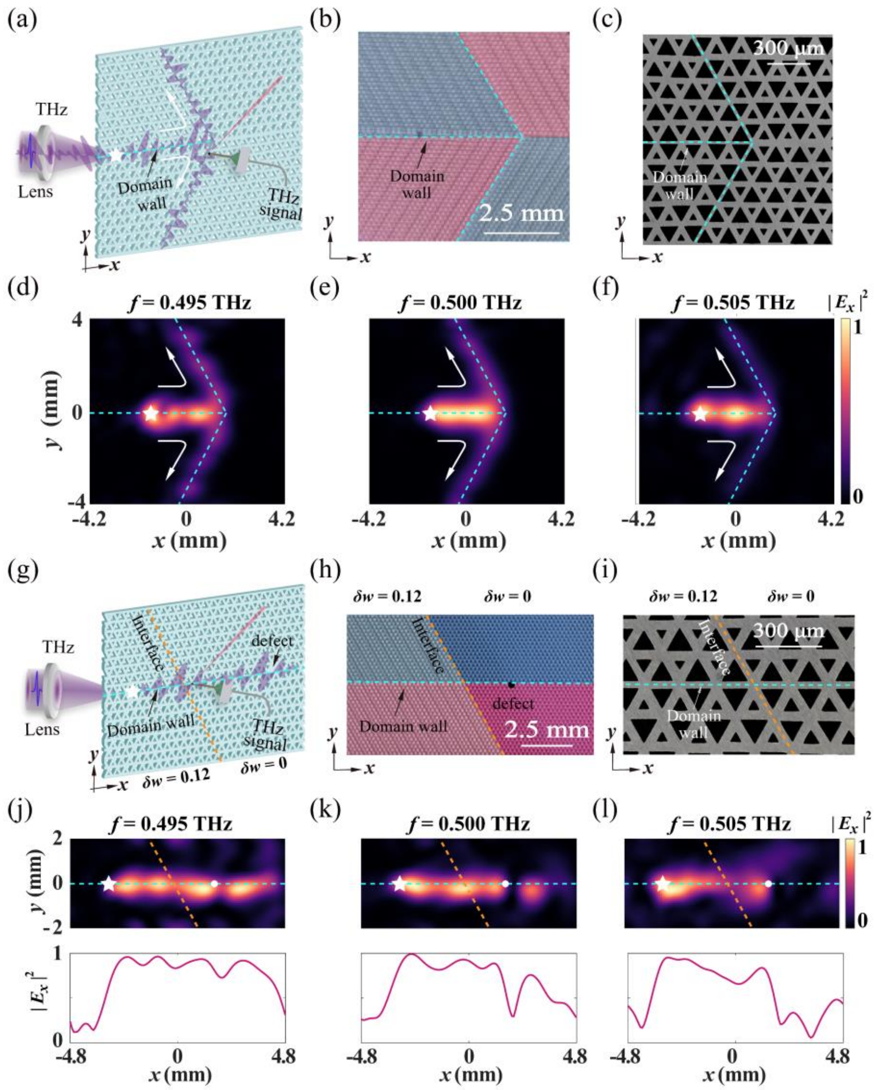

Figure R3.2 Measured electric-field intensity distributions of topological valley QBICs in the on-chip splitter and junction structures. (a) Schematic of the time-domain terahertz near-field scanning system used to record the electric-field distributions of the splitter design based on the compound VPC with $\delta w = 0.12$. (b) Optical image of the splitter sample. The red and blue regions represent compound VPCs with opposite Chern numbers. (c) Enlarged view of the splitter sample. (d to f) Measured electric-field intensity distributions of the splitter at 0.495 THz (d), 0.500 THz (e), and 0.505 THz (f). The cyan dashed lines indicate the positions of the domain walls in the compound VPCs. The white dots indicate the excitation positions. (g) Schematic of the time-domain terahertz near-field scanning system used to record the electric-field distributions of the junction between a compound VPC with $\delta w = 0.12$ and an unmodulated VPC with $\delta w = 0$. (h) Optical image of the junction sample. The red and blue regions represent VPCs with opposite Chern numbers. (i) Enlarged view of the junction sample. (j to l) Measured electric-field intensity distributions of the junction design at 0.495 THz (j), 0.500 THz (k), and 0.505 THz (l). The lower panels show the corresponding electric-field intensity profiles along the x axis at $y = 0$ mm.

In summary, we have modified the title, abstract, and introduction to clarify our motivation and advantages on page 1, lines 1 and 2: "Topological valley quasi-bound states in the continuum for radiatively accessible robust transport", page 1, lines 18 to 32: "Topological valley photonics enables on-chip light transport robust against backscattering, but valley edge states typically lie outside the light cone and cannot be directly excited from free space. Existing devices with radiative functionality mainly exploit on-chip–to–free-space emission through strongly leaky modes, where enhanced radiative coupling compromises transport performance. Achieving free-space–to–on-chip excitation while preserving low-loss topological transport therefore remains a challenge. Here, we experimentally demonstrate topological valley quasi-bound states in the continuum (QBICs) in terahertz valley photonic crystals. By introducing geometric modulation and Brillouin-zone folding, valley edge states are folded into the light cone and transformed into topological valley QBICs with controllable radiative coupling while preserving robust valley transport. Using time-domain terahertz near-field imaging, we directly visualize their transport and demonstrate tunable propagation lengths together with robust transport through sharp bends. We further realize on-chip routing functionalities based on junction and splitter architectures, illustrating free-space–to–on-chip excitation and subsequent signal processing. Our work establishes topological valley QBICs as a platform for interfacing free-space radiation with low-loss topological transport, opening new opportunities for integrated terahertz devices.", page 2, lines 9 to 13: "Existing devices with radiative functionality have consequently exploited strongly leaky edge states for on-chip-to-free-space emission[18]. While such approaches enable efficient radiation, the associated low Q factors and short propagation lengths limit their suitability for low-loss topological transport. Achieving free-space-to-on-chip excitation while preserving robust transport therefore remains a challenge.", page 2, lines 24 to 32: "Here, we experimentally demonstrate topological valley QBICs as radiative gateways for free-space-to-on-chip topological transport in terahertz compound VPCs. By introducing geometric modulation, we fold topological valley edge states into the light cone through Brillouin-zone folding and transform them into QBIC modes with controllable radiative coupling. Using time-domain terahertz near-field imaging (Figs. 1a and b), we directly visualize their real-space propagation, demonstrate geometry-tunable propagation lengths, and observe robust propagation through sharp bends. Junction and splitter architectures further show that the free-space-excited QBICs can be routed on chip for subsequent processing. Our work establishes topological valley QBICs as a platform for interfacing free-space radiation with low-loss topological transport." and added the junction and splitter architectures to the revised manuscript on page 5, lines 50 to 56, and page 6, lines 1 to 10. The original Fig. R3.2 has also been incorporated as Fig. 5 in the revised manuscript. Furthermore, the discussion of the Type-A design has been added as a new Supplementary Note, "Note 7. The Type-A design in Ref. [S1]" in the revised Supplementary Material.

<u>Reviewer 3 – Comment 2:</u>

2. Lack of experimental validation for the claimed QBIC properties

The defining figure of merit for qBICs is the quality (Q) factor, yet all analysis of Q factors in this manuscript is purely based on numerical simulations, with no experimental verification

(direct or indirect) provided. This is a critical gap, as the entire premise of the work relies on the realization of topological valley qBICs. To validate the QBIC characteristics experimentally, the authors should at least perform one of the following: (1) Far-field angle-resolved transmission/reflection spectroscopy, the standard and widely accepted characterization method in the qBIC field, to directly extract the experimental Q factors of the demonstrated resonances; (2) Quantitative analysis of propagation loss from the near-field measurements to back-calculate the experimental Q factors. The authors themselves provide the analytical relation between propagation length L and Q factor (L=vgQ/(2πf0)) in the manuscript, which can be directly applied to the measured data.
Notably, the electric-field distributions presented in Fig. 3g-i cannot be used to quantify propagation loss, and even show an unphysical increase in electric-field intensity with propagation distance, which is most likely caused by reflection from the sample end facets. The authors can use time-gating on their time-domain near-field data to eliminate spurious reflections, and then quantitatively extract the intrinsic propagation loss of the topological valley qBIC modes, and thereby derive the experimental Q factors for direct comparison with simulations.

Response from authors:
We thank you for this constructive comment. Following your suggestion, we have adopted the second approach, namely propagation-loss analysis from near-field measurements, to retrieve the experimental Q factors and directly compare them with simulations.

For our domain-wall valley QBICs, far-field angle-resolved spectroscopy is not sufficient for extracting the intrinsic Q factors. In the far-field experiment, the incident terahertz beam has a finite beam waist, whereas the valley QBICs are localized along the narrow domain-wall region. Therefore, the spatial overlap between the incident beam and the valley QBICs is small, resulting in weak excitation efficiency and broadened measured resonances. Consequently, the Q factors that would be extracted from far-field spectra mainly reflect the effective radiative response under the experimental excitation condition, rather than the intrinsic Q factors of the valley QBICs.

As discussed in our response to Reviewer 2 Comment 4, **electric-field intensity fluctuations** can arise from several experimental factors. First, **fabrication imperfections** may introduce local defects along the domain wall, resulting in local scattering and field enhancement. Second, the original **etching depth** of 280 μm was much larger than the designed depth of 150 μm, which can lead to nonuniform etching and position-dependent side-etching effects across the sample. These effects modify the local geometry and influence the scattering loss of the edge states. Third, since one near-field scan typically takes approximately 16 hours, **dust deposition** on the sample surface and long-term experimental fluctuations may also affect the measured field intensity. Therefore, the observed intensity fluctuations are more likely associated with the experimental factors discussed above than with reflections from the sample end facets, as further supported by the measurements of the refabricated sample discussed below.

To obtain more reliable field distributions for propagation-length extraction, we refabricated the samples by reducing the **etching depth from 280 μm to 180 μm** to suppress side-etching effects, optimized the near-field measurement system, and performed measurements. The improved measured electric-field intensity distributions used for propagation-length fitting are shown in Figs. R3.3a to f, which correspond to Figs. R2.4d to i.

The propagation length is extracted from the measured near-field distributions by fitting the electric-field intensity profile along the propagation direction using $|E(x)|^2 \propto \exp(-x/L)$, where x is the coordinate, and L is the propagation length. The corresponding Q factor is then obtained as $Q = 2\pi f_0 L/v_g$, where f_0 is the operating frequency and v_g is the group velocity. Since the experimentally measured projected dispersions are consistent with the simulated results, v_g is extracted from the simulated dispersion curves. For the compound VPCs with δw = 0.18, 0.15, and 0.12 at 0.499 THz, the fitted propagation lengths are 1.73 mm, 7.64 mm, and 17.22 mm, respectively, as shown in Figs. R3.3a to c. The corresponding **retrieved *Q* factors** are **119.43**, **456.86**, and **958.89**, respectively. The corresponding **simulated *Q* factors** are **126.95**, **753.77**, and **3208.60**, respectively. For the compound VPC with δw = 0.18, the fitted propagation lengths at 0.503 THz, 0.507 THz, and 0.511 THz are 2.20 mm, 4.64 mm, and 30.53 mm, respectively, as shown in Figs. R3.3d to f. The corresponding **retrieved *Q* factors** are **143.48**, **291.45**, and **1864.30**, respectively. Meanwhile, the corresponding **simulated *Q* factors** are **156.32**, **467.34**, and **864.74**, respectively.

The differences between the experimentally retrieved and simulated *Q* factors may be caused by fabrication-induced additional radiative loss and variations in the fitted propagation length. The experimentally retrieved *Q* factors can be lower than the simulated values because residual side-etching and other fabrication imperfections may introduce additional scattering and radiation loss that are not fully captured in the idealized simulations. In contrast, when the experimentally retrieved *Q* factors are higher than the simulated values, the larger values may be associated with variations in the fitted propagation length caused by local field variations. Dust deposition during long-time scans, fabrication defects along the domain wall, and residual field fluctuations can locally modify the measured electric-field intensity profiles, thereby affecting the exponential fitting of the propagation length and leading to larger retrieved *Q* factors.

These results show that the experimentally retrieved *Q* factors increase as the perturbation strength δw decreases, consistent with the QBIC behavior, and thereby provide quantitative experimental validation of the valley QBIC properties.

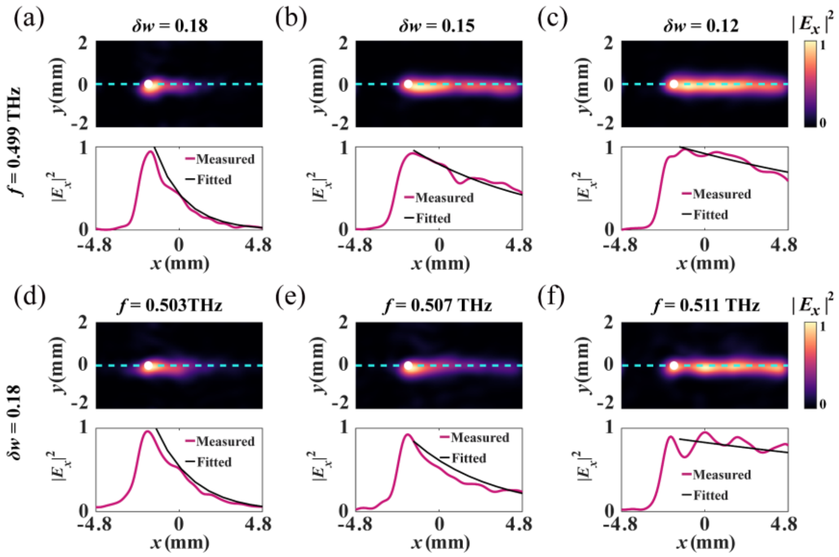

Figure R3.3 Measured electric-field intensity distributions of the topological valley QBICs in the compound VPCs with different δw and corresponding fitted results. (a to c) The electric-field intensity distributions of the topological valley QBICs in our compound VPCs at 0.499 THz with δw = 0.18 (a), 0.15 (b), and 0.12 (c), respectively. The red lines in the lower panels indicate the corresponding electric-field intensity distributions of the topological valley QBICs in the corresponding compound VPCs along the *x*-axis at y = 0 mm, respectively. The black lines in the lower panels indicate the corresponding fitted results, respectively. (d to f) The electric-field intensity distributions of the topological valley QBICs in the compound VPC with δw = 0.18 at 0.503 THz (d), 0.507 THz (e), and 0.511 THz (f), respectively. The red lines in the lower panels indicate the corresponding electric-field intensity distributions of the topological valley QBICs in the corresponding compound VPCs along the *x*-axis at y = 0 mm, respectively. The black lines in the lower panels indicate the corresponding fitted results, respectively.

In summary, we have added the above discussion on page 4, lines 45 to 49: "We extract the propagation lengths from the measured near-field distributions by fitting the electric-field intensity profile along the propagation direction. We fit the propagation length using $|E(x)|^2 \propto \exp(-x/L)$, where x is the coordinate and L is the propagation length. The fitted propagation lengths are 1.73 mm, 7.64 mm, and 17.22 mm for δw = 0.18, 0.15, and 0.12 at 0.499 THz, respectively.", page 4, lines 51 to 57, and page 5, lines 1 to 5: "The corresponding Q factor is then obtained as $Q = 2\pi f_0 L/v_g$, where f_0 is the operating frequency and v_g is the group velocity. The group velocity is extracted from the simulated dispersion because the measured projected dispersions are consistent with the simulated ones. The retrieved Q factors for the compound VPCs with δw = 0.18, 0.15, and 0.12 at 0.499 THz are 119.43, 456.86, and 958.89, respectively. The corresponding simulated Q factors are 126.95, 753.77, and 3208.60, respectively. These results show that the overall propagation length and retrieved Q factor increase as the perturbation strength δw decreases, consistent with the QBIC behavior. For the compound VPC with δw = 0.18, the propagation length and retrieved Q factor also increase with increasing operating frequency within the measured frequency range. The differences between the experimentally retrieved and simulated Q factors may be caused by fabrication-induced additional radiative loss and variations in the fitted propagation length (Note 3 for details)." in the revised manuscript.

Reviewer 3 – Comment 3:

3. Lack of quantitative experimental verification of topological protection

The geometric modulation introduced in this work breaks the translational symmetry of the original lattice, which will inevitably induce mixing between counter-propagating edge states. Specifically, at kx=0, the opening of a gap indicates that the mode comprises equal (50%) contributions from the K and K' valleys; even at non-zero kx, the mode is never 100% a single valley component. This mixing directly undermines the valley Hall topological protection that is the foundation of the claimed robust transport. However, the manuscript only provides a qualitative demonstration of backscattering-free transport along a sharp bend, with no quantitative experimental evidence to validate the retention of topological protection. Leveraging their time-resolved near-field measurements, the authors should be able to extract the momentum-space distributions of the modes at different frequencies and propagation times, quantitatively analyze the valley composition of the demonstrated states, and rigorously verify the degree to which topological protection is preserved in this system.

Response from authors:

We thank you for this insightful and technical comment. We agree that "*The geometric modulation introduced in this work breaks the translational symmetry of the original lattice, which will inevitably induce mixing between counter-propagating edge states.*". In particular, near the folded Γ point, the opening of a small gap indicates the coupling between the K and K' valley components. Similar behavior has also been observed in valley-Hall-type systems, such as the Wu–Hu model [S3.2], where a small gap can appear due to weak valley coupling while robust edge-state transport is still preserved.

In our system, by introducing small δw, the intervalley coupling remains weak away from the folded Γ point, such that valley polarization is largely preserved, and backscattering is strongly suppressed.

Following your suggestion, we performed a quantitative analysis of the valley composition using the experimentally measured near-field distributions. Specifically, we extracted the momentum-space field distributions through spatial Fourier transform of the measured complex near-field data and evaluated the spectral intensities around the folded K and K' valleys originating from the unmodulated VPC. We then define the **valley-polarization contrast coefficient** as $\eta = (I_K - I_{K'})/(I_K + I_{K'})$, where I_K and $I_{K'}$ are the integrated spectral intensities around the K and K' valleys, respectively.

As shown in Fig. R3.4, the extracted **valley-polarization contrast coefficient remains high**, with $\eta > 0.75$, for the compound VPC with $\delta w = 0.12$ at 0.490, 0.495, and 0.500 THz **during propagation through the Z-bend domain wall**. More importantly, the valley polarization before and after the bending region shows negligible redistribution between the K and K' components, indicating weak intervalley scattering during propagation. These results provide quantitative experimental evidence that the valley polarization of the edge states is largely retained despite the supercell modulation and Brillouin-zone folding.

Therefore, although finite valley mixing is introduced by the geometric modulation, **robust valley-polarized transport** is still experimentally **observed**.

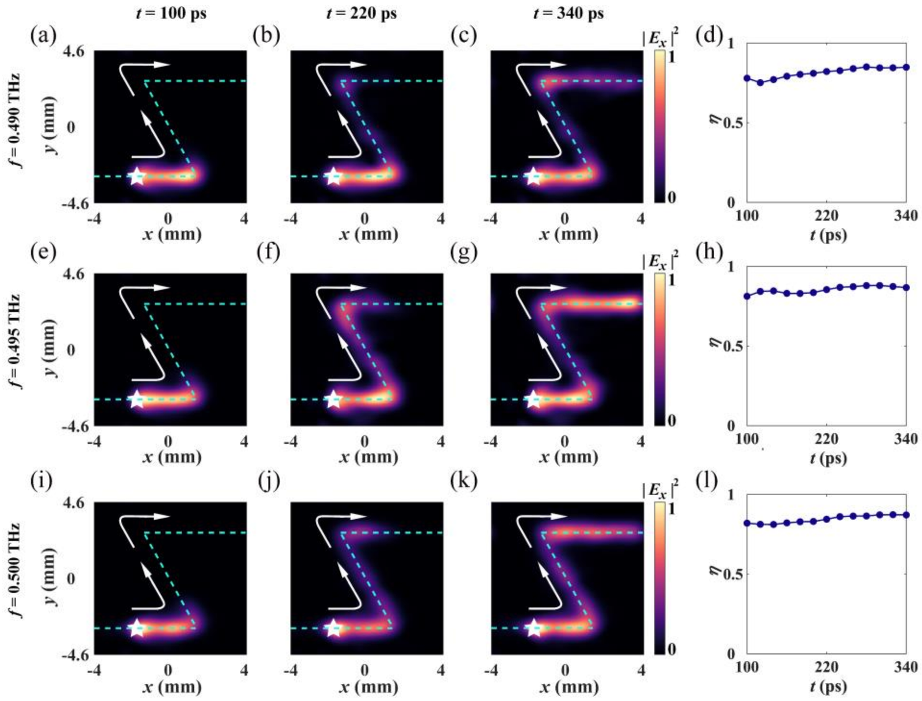

Figure R3.4 Extracted measured electric-field intensity distributions and corresponding valley-polarization contrast coefficient η. (a to c) Extracted measured electric-field intensity distributions of the Z-bend domain wall with $\delta w = 0.12$ at 0.490 THz at different time delays during propagation. (d) Corresponding valley-polarization contrast coefficient η as a function of time delay. (e to g) Extracted measured electric-field intensity distributions of the Z-bend domain wall with $\delta w = 0.12$ at 0.495 THz at different time delays during propagation. (h) Corresponding valley-polarization contrast coefficient η as a function of time delay. (i to k) Extracted measured electric-field intensity distributions of the Z-bend domain wall with $\delta w = 0.12$ at 0.500 THz at different time delays during propagation. (l) Corresponding valley-polarization contrast coefficient η as a function of time delay.

In summary, we have added the above discussion on page 5, lines 24 to 49: "We fabricate a compound VPC with $\delta w = 0.12$ that forms a Z-bend domain wall, as shown in the optical image in Fig. 4b. The red and blue regions correspond to compound VPCs with opposite valley Chern numbers. Figures 4c and d show enlarged views of the bending region and the upper section of the domain wall, respectively. Figures 4e and f illustrate the extracted simulated electric-field intensity distributions of the topological valley QBICs at 0.495 THz after excitation for 100 ps and 340 ps, respectively, indicating robust propagation through the Z-bend domain wall. To demonstrate robust transport of the valley QBICs, we perform a two-dimensional Fourier transform of the measured complex near-field distributions. The orange dashed lines denote the Brillouin-zone boundary of the unmodulated VPC ($\delta w = 0$), whereas the white lines represent the Brillouin-zone boundaries of the compound VPC ($\delta w \neq 0$). The reciprocal lattice vectors of the compound VPC are indicated by $\mathbf{b}_1$ and $\mathbf{b}_2$. Two dominant momentum components are observed in the Brillouin zone of the compound VPC, corresponding to the folded K and K'

valleys originating from the unmodulated VPC (Fig. 4g). We then define the valley-polarization contrast coefficient as $\eta = (I_K - I_{K'})/(I_K + I_{K'})$, where I_K and $I_{K'}$ are the integrated spectral intensities around the folded K and K' valleys, respectively. The extracted simulated valley polarization contrast coefficient remains nearly unchanged during propagation (Fig. 4h), indicating suppressed intervalley scattering and robust transport through the Z-bend domain wall (Note 4 for details). By analyzing the measured time-domain near-field signals, we directly visualize the propagation of the topological valley QBICs through the Z-bend domain wall (Figs. 4i and j). The measured valley QBICs propagate along the bent domain wall at 0.495 THz while maintaining strong confinement, with suppressed scattering into bulk modes. Consistently, two dominant momentum components are observed in the measured Brillouin-zone distribution of the compound VPC with δw = 0.12 (Fig. 4k), in agreement with the simulated results in Fig. 4g. The experimentally extracted valley-polarization contrast coefficient η remains stable during propagation through the Z-bend, as shown in Fig. 4l, indicating that the valley polarization is largely retained despite finite valley mixing. This result demonstrates robust valley-polarized transport in the Z-bend domain wall.", updated Fig. 4 in the revised manuscript and added the Fig. R3.4 as a new Supplementary Note: "Note 4. Robust transport" in the revised Supplementary Material.

Reviewer 3 – Comment 4:

Specific and Technical Comments:

1. Universality of the Brillouin-zone folding mechanism for arbitrary propagation directions

As shown in Fig. 2a, the authors apply geometric modulation along the x-direction to the entire bulk region, breaking translational symmetry along x. While this scheme works for valley edge states propagating along the x-direction, it is unclear whether this x-direction modulation can fold the band structures of valley edge states propagating along other directions in the same manner—for example, the bent waveguide path along the −1/2 x+3/2 y direction shown in Fig. 4. The authors must supplement theoretical analysis and numerical simulations to clarify the physical origin and universality of the Brillouin-zone folding mechanism for edge states along arbitrary propagation directions.

Response from authors:

We thank you for this constructive comment. The x-direction modulation does ***not*** fold the band structures of edge states propagating along the bent domain-wall direction.

The bent domain wall direction mentioned by the reviewer corresponds to the $\boldsymbol{d} = (-1/2, \sqrt{3}/2)$ direction in our coordinate convention. In our work, a supercell modulation with period P is introduced along the x-direction, as shown in Fig. R3.5a. The lattice vectors change from $\boldsymbol{a}_{VPC,1} = (1,0)P/3$, $\boldsymbol{a}_{VPC,2} = (-1/2, \sqrt{3}/2)P/3$ (VPC) for the unmodulated VPC to $\boldsymbol{a}_1 = (1,0)P$, $\boldsymbol{a}_2 = (-1/2, \sqrt{3}/2)P/3$ for the compound VPC, respectively. The corresponding reciprocal lattice vectors change from $\boldsymbol{b}_{VPC,1} = (\frac{6\pi}{P}, \frac{6\pi}{\sqrt{3}P})$, $\boldsymbol{b}_{VPC,2} = (0, \frac{12\pi}{\sqrt{3}P})$ (VPC) for the unmodulated VPC to $\boldsymbol{b}_1 = (\frac{2\pi}{P}, \frac{2\pi}{\sqrt{3}P})$, $\boldsymbol{b}_2 = (0, \frac{12\pi}{\sqrt{3}P})$ for the compound VPC, respectively. Therefore, the Brillouin-zone boundary associated with $\boldsymbol{b}_1$ is folded, whereas the boundary associated with $\boldsymbol{b}_2$ remains unchanged.

According to the relation between the lattice vectors and reciprocal lattice vectors $\boldsymbol{a}_i \cdot \boldsymbol{b}_j = 2\pi\delta_{ij}$, we obtain $\boldsymbol{a}_2 \cdot \boldsymbol{b}_1 = 0$ and $\boldsymbol{a}_2 \cdot \boldsymbol{b}_2 = 2\pi$. Since the vector $\boldsymbol{d}$ is parallel to $\boldsymbol{a}_{VPC,2}$ and $\boldsymbol{a}_2$, the unchanged lattice vector $\boldsymbol{a}_2$ and reciprocal vector $\boldsymbol{b}_2$ determine the Brillouin-zone boundary relevant to edge states propagating along the $\boldsymbol{d}$-direction. Therefore, no Brillouin-zone folding occurs for the edge-state dispersion along the $\boldsymbol{d}$-direction, as shown in Fig. R3.5b. Figure R3.5c illustrates the corresponding simulated edge-state dispersion along the $\boldsymbol{d}$-direction.

Consequently, introducing geometric modulation in one lattice vector direction does **not universally** induce **Brillouin-zone folding** for **all lattice vector directions**.

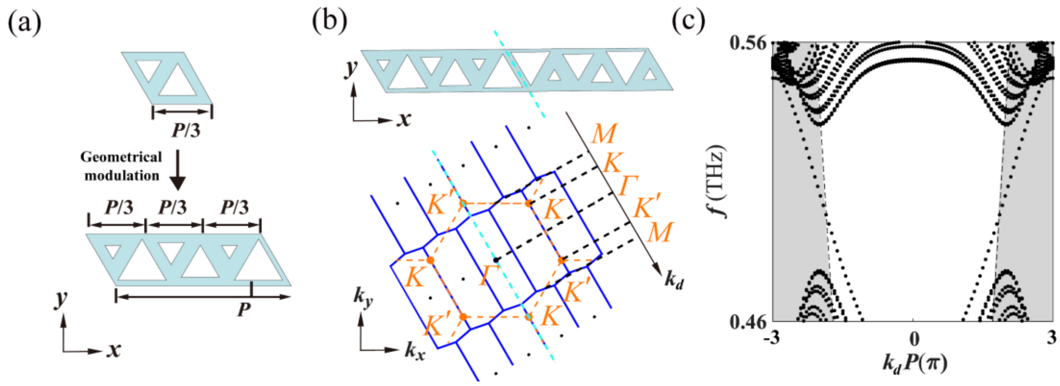

Figure R3.5 A modulated VPC with a domain wall along the $\boldsymbol{d} = (-1/2, \sqrt{3}/2)$ direction. (a) Schematic of the unit cell with geometric modulation introduced along the *x*-direction. (b) Corresponding two-dimensional Brillouin zone and projected domain-wall direction along $\boldsymbol{d} = (-1/2, \sqrt{3}/2)$ direction. (c) Dispersion of the domain wall in (b). The gray shaded region indicates the light cone.

In summary, we have added the above discussion as a new Supplementary Note: "Note 8. Dispersion of the domain wall along $\boldsymbol{d} = (-1/2, \sqrt{3}/2)$ direction" in the revised Supplementary Material.

Reviewer 3 – Comment 5:

2. Quantitative comparison between simulated and experimental Q factors for the measured samples

The authors fabricate and measure samples with δw=0.18, which corresponds to δw^−2≈30. According to the simulated results in Fig. 2e, the Q factor at this parameter should be approximately 2×10^5. The authors must explicitly report the experimentally measured Q factor for this sample, and provide a direct comparison and discussion of any discrepancies with the simulated value.

Response from authors:

We thank you for pointing this out.

First, we note that the horizontal axis in Fig. 2e spans δw^{-2} from 0 to 1000. For the fabricated sample with $\delta w = 0.18$, corresponding to $\delta w^{-2} \approx 30$, the sample lies close to the low-δw^{-2} side of Fig. 2e. Therefore, the relevant simulated Q factors for the measured sample are on the order of 10^2–10^3, as listed below. The much larger Q values in Fig. 2e occur closer to the high-δw^{-2} side, where the perturbation is weaker and the modes approach the quasi-BIC limit.

As discussed in our responses to your Comments 2 and 3, we refabricated the sample and optimized the near-field measurement system to improve the experimental results. We then fitted the propagation lengths from the improved measured near-field intensity distributions and extracted the corresponding Q factors for the fabricated samples. For the valley QBICs in the compound VPC with $\delta w = 0.18$, the experimentally **retrieved Q factors** are **143.48**, **291.45**, and **1864.30** at 0.503 THz, 0.507 THz, and 0.511 THz, respectively. The corresponding **simulated Q factors** are **156.32**, **467.34**, and **864.74**, respectively.

The differences between the experimentally retrieved and simulated Q factors may be caused by fabrication-induced additional radiative loss and variations in the fitted propagation length. The experimentally retrieved Q factors can be lower than the simulated values because residual side-etching and other fabrication imperfections may introduce additional scattering and radiation loss that are not fully captured in the idealized simulations. In contrast, when the experimentally retrieved Q factors are higher than the simulated values, the larger values may be associated with variations in the fitted propagation length caused by local field variations.

Dust deposition during long-time scans, fabrication defects along the domain wall, and residual field fluctuations can locally modify the measured electric-field intensity profiles, thereby affecting the exponential fitting of the propagation length and leading to larger retrieved Q factors.

Overall, the experimentally retrieved Q factors show the same increasing trend as the simulated values and are comparable in magnitude to those corresponding simulated values

In summary, we have added the above discussion on page 5, lines 5 to 15: "Figures 3j to l illustrate the electric-field intensity distributions of the topological valley QBICs in the compound VPC with δw = 0.18 at 0.503 THz, 0.507 THz, and 0.511 THz, respectively. The corresponding fitted propagation lengths are 2.20 mm, 4.64 mm, and 30.53 mm, respectively. The propagation lengths of the topological valley QBICs in the compound VPC with δw = 0.18 also gradually increase at these frequencies. This is consistent with the simulations shown in Fig. 2d. The retrieved Q factors are 143.48, 291.45, and 1864.30 for the valley QBICs in our compound VPCs with δw = 0.18 at 0.503 THz, 0.507 THz, and 0.511 THz, respectively. Meanwhile, the corresponding simulated Q factors are 156.32, 467.34, and 864.74, respectively. We also retrieve Q factors for more frequencies of the compound VPCs with δw = 0.18, 0.15, and 0.12, respectively (Note 3 for details). Overall, the experimentally retrieved Q factors show the same increasing trend as the simulated values and are comparable in magnitude." in the revised manuscript.

<u>Reviewer 3 – Comment 6:</u>
3. Quantitative analysis of Q factors from the measured dispersion bands
The experimentally measured projected dispersions in Fig. 3d-f exhibit significant linewidth broadening, which implies markedly lower Q factors than the ultrahigh values predicted in simulations. The authors should perform quantitative fitting of the measured dispersion bands to extract the experimental Q factors at different momenta, and explain the origin of the discrepancy between experimental and simulated results.

<u>Response from authors:</u>
We thank you for pointing this out. This comment is related to Reviewer 2 Comment 3. The measured projected dispersions in Figs. 3d to f are obtained by applying a two-dimensional spatial Fourier transform to the measured near-field electric-field distributions. These maps reveal the momentum-resolved spectral intensity of the excited near-field response, but their apparent linewidths may not reliably reflect the intrinsic modal linewidths of the valley QBICs. This is because the linewidths can be broadened by the finite temporal and spatial measurement windows, Fourier-transform resolution, excitation-beam momentum spread, probe response, and near-field intensity fluctuations. Therefore, direct linewidth fitting of the measured projected dispersion bands may not provide a reliable estimate of the intrinsic Q factors. Instead, we retrieve the experimental Q factors from the fitted propagation lengths of the measured electric-field intensity profiles, which are directly related to the modal lifetime through $Q = 2\pi f_0 L/v_g$.

As discussed in our response to your Comment 2, we have fitted the propagation length from electric-field measurements by using $|E(x)|^2 \propto \exp(-x/L)$, where x is the coordinate, and L is the propagation length. Then, we retrieved the experimental Q factors. In the following, we perform the propagation length fitting to different samples to retrieve the experimental Q factors at different frequencies, which correspond to different momenta.

Figure R3.6 illustrates the measured electric-field intensity distributions and the corresponding fitted propagation lengths for the compound VPCs with δw = 0.18, 0.15, and 0.12, respectively. Figures R3.6a to g show the electric-field intensity distributions of the topological valley QBICs in the compound VPC with δw = 0.18 from 0.497 THz to 0.512 THz, with a frequency increment of 0.0025 THz. The corresponding **fitted propagation lengths** are **1.88 mm**, **1.73 mm**, **1.84**

mm, **2.57 mm**, **4.64 mm**, **7.04 mm**, and **12.85 mm**, respectively. Figures R3.6h to n show the electric-field intensity distributions of the topological valley QBICs in the compound VPC with δw = 0.15 from 0.489 THz to 0.504 THz, with a frequency increment of 0.0025 THz. The corresponding **fitted propagation lengths** are **3.27 mm**, **2.92 mm**, **2.37 mm**, **4.17 mm**, **7.65 mm**, **15.29 mm**, and **17.66 mm**, respectively. Figures R3.6o to u show the electric-field intensity distributions of the topological valley QBICs in the compound VPC with δw = 0.12 from 0.485 THz to 0.500 THz, with a frequency increment of 0.0025 THz. The corresponding **fitted propagation lengths** are **3.34 mm**, **3.50 mm**, **7.41 mm**, **11.79 mm**, **18.28 mm**, **7.08 mm**, and **56.34 mm**, respectively. In each lower panel, the red curves represent the extracted electric-field intensity profiles of the corresponding topological valley QBICs along the x-axis at y = 0 mm, while the black curves represent the exponential fitting used to determine the propagation length.

Figure R3.7 illustrates the retrieved Q factors for the compound VPCs with δw = 0.18, 0.15, and 0.12, respectively. As discussed in our response to your Comment 5, the differences between the experimentally retrieved and simulated Q factors may be caused by fabrication-induced additional radiative loss and variations in the fitted propagation length. The experimentally retrieved Q factors can be lower than the simulated values because residual side-etching and other fabrication imperfections may introduce additional scattering and radiation loss that are not fully captured in the idealized simulations. In contrast, when the experimentally retrieved Q factors are higher than the simulated values, the larger values may be associated with variations in the fitted propagation length caused by local field variations. Dust deposition during long-time scans, fabrication defects along the domain wall, and residual field fluctuations can locally modify the measured electric-field intensity profiles, thereby affecting the exponential fitting of the propagation length and leading to larger retrieved Q factors.

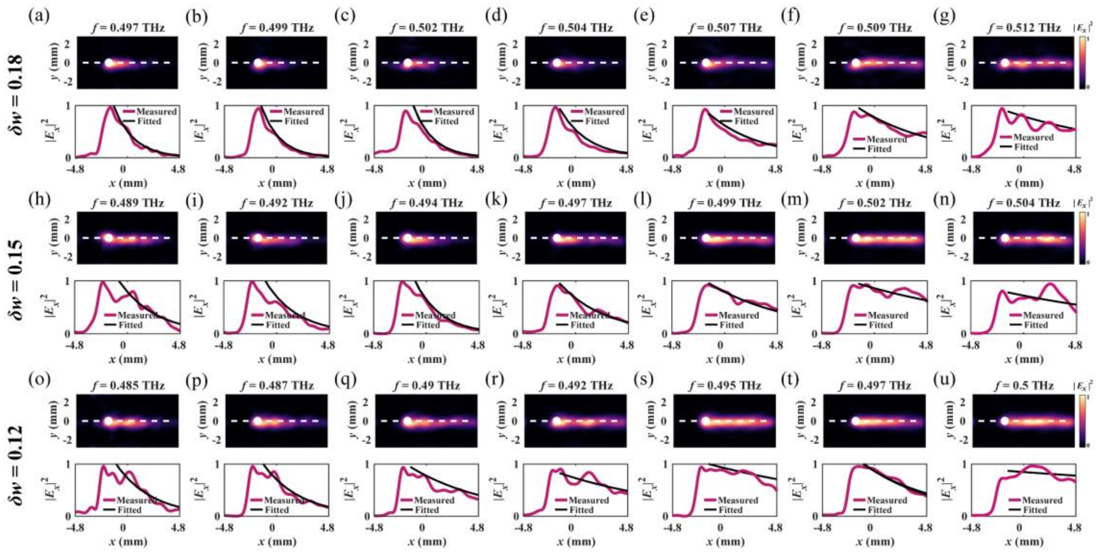

Figure R3.6 Measured electric-field intensity distributions and fitted propagation lengths for compound VPCs with different δw. (a to g) Measured electric-field intensity distributions of the topological valley QBIC modes in the compound VPC with δw = 0.18 from 0.497 THz to 0.512 THz, with a frequency increment of 0.0025 THz. (h to n) Measured electric-field intensity distributions of the topological valley QBIC modes in the compound VPC with δw = 0.15 from 0.489 THz to 0.504 THz, with a frequency increment of 0.0025 THz. (o to u) Measured electric-field intensity distributions of the topological valley QBIC modes in the compound VPC with δw = 0.12 from 0.485 THz to 0.500 THz, with a frequency increment of 0.0025 THz. In each lower panel, the red curves represent the extracted electric-field intensity profile of the corresponding topological valley QBIC mode along the x-axis at y = 0 mm, while the black curves represent the exponential fitting used to determine the propagation length.

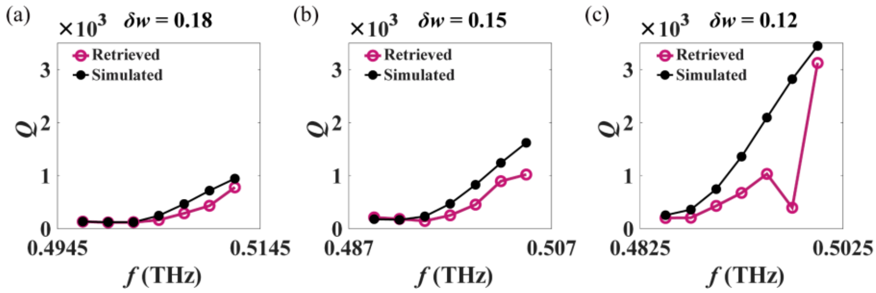

Figure R3.7 Retrieved Q factors for compound VPCs with different δw. (a to c) Retrieved Q factors for the compound VPCs with δw = 0.18, 0.15, and 0.12, respectively. The red circles and black dots represent the experimentally retrieved and simulated Q factors, respectively.

In summary, we have added the above discussion on page 5, lines 12 to 14: "We also retrieve Q factors for more frequencies of the compound VPCs with δw = 0.18, 0.15, and 0.12, respectively (Note 3 for details)." in the revised manuscript and added Figs. R3.6 and R3.7 as Figs. S4 and S5 in Note 3 in the Supplementary Material.

Reviewer 3 – Comment 7:

Overall, the concept of topological valley QBICs proposed in this manuscript is of some potential interest to the photonics community. However, I feel the manuscript currently has two critical shortcomings: (1) the limited novelty of this work compared to prior literature, and (2) the absence of key experimental validation for the core claims of qBIC characteristics and topological protection. Considering the rigorous standards required for publication in Nature Communications, I suggest authors to comprehensively address these problems.

Response from authors:

We thank you for your careful evaluation of our manuscript and for pointing out the key issues regarding novelty and experimental validation. Following your comments, we have carefully revised the manuscript and Supplementary Material, and have added substantial theoretical analyses, numerical simulations, and experimental results to clarify the physical mechanism and strengthen the evidence supporting our claims.

We would like to briefly summarize the main novelty and advances of the revised manuscript as follows.

(1) **Realization of terahertz-regime topological valley QBICs through Brillouin-zone folding of on-chip valley edge states.** In our approach, originally non-radiative valley edge states below the light cone are folded into the light cone by introducing a controlled geometric modulation, thereby transforming them into radiatively accessible topological valley QBICs.

(2) **Experimental demonstration of tunable Q factors, evidenced by Q-factor-dependent on-chip propagation lengths.** By measuring the near-field electric-field distributions, we extract propagation lengths and retrieve the corresponding experimental Q factors, showing that the Q factors and propagation lengths can be tuned by the geometric perturbation strength.

(3) **Demonstration of a new approach for bridging free-space propagating waves and on-chip topological edge states.** The valley QBICs serve as radiative gateways that enable free-space-to-on-chip excitation while maintaining robust valley transport, and the newly added junction and splitter architectures further demonstrate their potential for on-chip signal routing and processing.

In summary, these revisions directly address the concerns regarding both the novelty of our work and the experimental validation of the QBIC characteristics and topological robustness.

Reference

S3.1 Wang W. et al., On-chip topological leaky-wave antenna for full-space terahertz wireless connectivity. *Nat. Photon.* **20**, 317–323 (2026).

S3.2 Wu L., and Hu X., Scheme for Achieving a Topological Photonic Crystal by Using Dielectric Material. *Phys. Rev. Lett.* **114**, 223901 (2015).

Response Letter to Reviewers

We are grateful for your constructive comments on this manuscript (NCOMMS-26-011646A).

In the text below, your comments are quoted in *Italics* and followed by our detailed response. We have also revised the manuscript based on your comments, and these updates are highlighted in blue in the main text. In the text below, the references to these updates are highlighted in blue and also by a vertical red line in the left margin.

Response to Reviewer 1:

Reviewer 1 – General comments:

The authors have made commendable efforts to improve their manuscripts and to reply to the concerns raised in the first review round. The manuscript now makes a more convincing case for the radiatively accessible robust transport. Considering the revisions and improvements, I am happy to recommend publication in Nature Communications.

Response from authors:

We thank you for the positive evaluation of our revised manuscript. We appreciate your recognition of our efforts in improving the manuscript and addressing the concerns raised during the first round of review. We are grateful for your recommendation for publication in *Nature Communications*. Our responses to your improvement suggestions are provided below.

Reviewer 1 – Comment 1:

I made note of some improvement suggestions that appeared during revisions:

1, In Lines 76-81, the Hamiltonian equations are embedded in the text. For better readability, it is recommended to set these mathematical expressions as separate, numbered equation lines. c_{i}^{\dagger }, c_{i} should be the creation/annihilation operators, pleas clarify it in the maintext.

Response from authors:

We thank you for the constructive comment. Following your suggestion, we have reformatted the Hamiltonian expressions as separate numbered equations (Eqs. (1)–(4)) to improve readability. In addition, we have explicitly clarified in the main text that $c_i^\dagger$ and c_i denote the creation and annihilation operators, respectively.

In summary, we have revised the manuscript in Page 2, lines 37 to 49: "The Hamiltonian for a VPC is

$$H = -t\sum_{<ij>} c_i^\dagger c_j + \sum_i U_i c_i^\dagger c_i, \tag{1}$$

where $\sum_{<ij>}$ denotes the summation over nearest-neighbor pairs, t is the nearest-neighbor hopping, and $c_i^\dagger$ (c_i) denotes the creation (annihilation) operator at site i. The onsite potential U_i is given by

$$U_i = \begin{cases} U_1, i = 2n, \\ -U_1,\ i = 2n+1, \end{cases} \tag{2}$$

where n is an integer. After introducing onsite-potential modulation, the Hamiltonian for the compound VPC can be described as

$$H_{3P} = -t\sum_{<ij>} c_i^\dagger c_j + \sum_i U_i c_i^\dagger c_i + \sum_i \delta U_i c_i^\dagger c_i, \tag{3}$$

The onsite-potential modulation δU_i is given by

$$\delta U_i = \begin{cases} \delta U, i = 3n, \\ 0, i = 3n+1, \\ -\delta U, i = 3n+2, \end{cases} \quad (4)$$

where $\delta U = U_2 - U_1$ is the amplitude of the period-tripling onsite-potential modulation. Here, U_1 and U_2 denote the onsite potentials associated with the two different unit cells in the compound VPC."

Reviewer 1 – Comment 2:

2, While plotting Qvs \delta w^{-2} linearly is perfectly fine and shows the trend, in the BIC community, it is also common to plot Q vs δw on a log-log scale to explicitly show the slope of -2. The authors might consider if a log-log inset would visually reinforce the Q\propto \delta w^{-2}scaling law.

Response from authors:

We appreciate your suggestion. We have added a log-log inset in Fig. 2e in the main text as illustrated in Fig. R1.

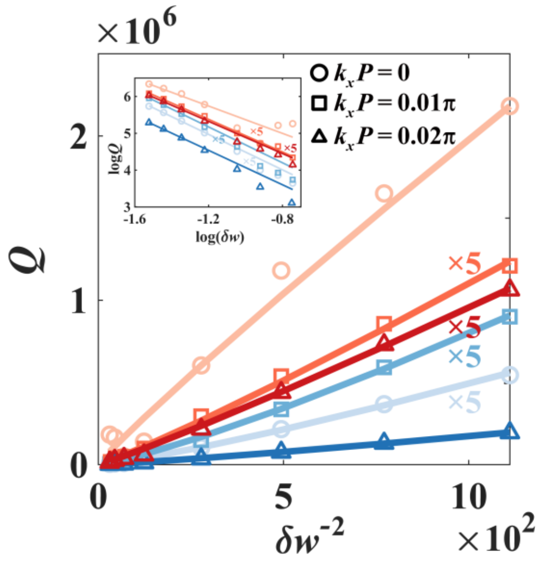

Fig. R1 Dependence of the Q factors of the topological valley QBICs on the inverse square of the geometric parameter δw for $k_x P = 0$ (circle), 0.01π (square), and 0.02π (triangle), respectively. The inset shows the same data on a log–log scale, demonstrating an approximately inverse-square dependence of the Q factor on the geometric parameter δw.

In summary, we have updated Figs. 2e in the revised manuscript.

Response to Reviewer 2:

Reviewer 2 – General comments:

The authors have addressed all of my previous comments satisfactorily. I appreciate their careful revisions and detailed responses. I have no further concerns and recommend this manuscript for publication in Nature Communications.

Response from authors:

We thank you for the positive evaluation of our revised manuscript. We appreciate your recognition that we have satisfactorily addressed all of your previous comments. We are grateful for your recommendation for publication in *Nature Communications*.

Response to Reviewer 3:

Reviewer 3 – General comments:
I appreciate the authors revision. Thr major claim of current version seems to be well supported by experimental results and analysis. I thus recommend its publication in Nature Communications.

Response from authors:
We thank you for the positive evaluation of our revised manuscript. We appreciate your recognition that the main claim of the manuscript is now well supported by the experimental results and analysis. We are grateful for your recommendation for publication in *Nature Communications*.